NOAA Technical Memorandum ERL PMEL-49

THE VARIATION OF THE DRAG COEFFICIENT IN THE MARINE SURFACE LAYER DUE TO TEMPORAL AND SPATIAL VARIATIONS OF THE SURFACE WIND AND SEA STATE

Hugh Michael Byrne

Pacific Marine Environmental Laboratory
Seattle, Washington
June 1983

UNITED STATES
DEPARTMENT OF COMMERCE
Malcolm Baldrige,
Secretary

NATIONAL OCEANIC AND
ATMOSPHERIC ADMINISTRATION
John V. Byrne,
Administrator

Environmental Research
Laboratories
George H. Ludwig
Director

NOTICE

Mention of a commercial company or product does not constitute an endorsement by NOAA Environmental Research Laboratories. Use for publicity or advertising purposes of information from this publication concerning proprietary products or the tests of such products is not authorized.

CONTENTS

TABLES

FIGURES

Figures Page

Figures Page

The Variation of the Drag Coefficient in the Marine Surface Layer Due to Temporal and Spatial Variations of the Surface Wind and Sea State*

Hugh Michael Byrne**

ABSTRACT. The neutral atmospheric drag coefficient, C_{dn}, and ocean surface wave spectra were measured on both sides of a strong atmospheric front. The front was part of a mature extratropical cyclone moving across the Gulf of Alaska on 15 November 1980. Results showed a large variation in C_{dn} at constant mean wind speed in the cold sector which could not be explained by formulations found in the literature.

Previous work which attempted to relate drag coefficients to surface wind speed paid slight attention to the coincident surface wave field. As a result, no explicit dependence of C_{dn} on the wave field has ever been reported. This investigation, which measured the complete one-dimensional surface wave spectrum, constitutes the first time wave spectral measurements have been made together with eddy correlation flux measurements in the marine surface layer. Coincident wave spectral measurements showed an unexpected increase in energy in the six-second wave band (.15→.17 hz), which was correlated with the variation of C_{dn}. The spatial distribution of wave spectral energy in the duration-limited sea behind the 15 November front was found to differ markedly from the spatial distribution of wave spectral energy in the fetch limited case. The wave spectra in the warm sector followed Phillips' model well. The wave spectra in the cold sector did not.

Using only the wave spectral information, a representation of z_o, was derived which reduced to Charnock's relation in situations of dynamic equilibrium between the wind field and the surface waves. In situations of disequilibrium between the wave field and the surface wind, the derived relation showed a dependence of z_o on the six-second wave field. We found that C_{dn} calculated from measurements made during the 15 November 1980 frontal penetration, and the 7 November post-frontal flight followed the derived z_o relationship. This relationship of z_o to the surface wave spectra helps explain the high values of C_{dn} behind moving fronts which have been reported in the literature.

---

* Contribution number 621 from the Pacific Marine Environmental Laboratory.

**Present address: TASC, One Jacob Way, Reading, Massachusetts 01867

1. CHAPTER I: INTRODUCTION

As early as 1916, G. I. Taylor reasoned that the horizontal interaction between the Earth's surface and the moving atmosphere might be represented by a velocity-square law involving a nondimensional factor known as the *drag coefficient*, C_d. In the succeeding years, comprehensive observations have verified that, although the square law generally applies over land, over the sea, it is still a matter of contention. At the same time, advances made in turbulence theories, and the advent of similarity theories for both the atmospheric surface and boundary layers allow the drag coefficient to be explicitly defined in terms of aerodynamic roughness, atmospheric stability, and other relevent parameters.

In general, micrometeorologists have concluded, through wind profile observations and direct measurements of Reynolds stresses, that the drag coefficient is nearly constant or a slowly increasing function of wind speed (Large and Pond, 1980), and that it is a factor of two or three smaller than needed to bring the computed results of numerical models into close agreement with observations (Donelan, 1982).

It is interesting to note that, whereas most determinations of C_d are done under conditions of horizontal homogeneity and steady state, most models are verified using "significant events" usually associated with rapid changes in the wind such that the wave field is either young or moving against the wind.

Recent work indicated that some of this discrepency may be due to the preference of micrometeorologists for steady wind conditions for their measurements. As a result, their over-the-oceans measurements are biased towards a fully developed wave field. It has been shown that the drag coefficient approaches a pronounced minimum as the wave field approaches maturity (Kitaigorodskii, 1970; Krauss, 1967).

This investigation approached the problem of measuring the drag coefficient in regions where there are temporal and spatial variations of the surface wind and sea state. Our goal was to provide more realistic representation of the drag coefficient in the turning-wind condition which would allow greater accuracy in calculation of the momentum exchange and heat and water vapor fluxes during a storm passage over the ocean.

The major effort involved measuring by the correlation method, the Reynolds stress in the marine boundary layer close to a moving atmospheric front. The Reynolds stress measurement was correlated with the bulk surface-layer meteorological measurements together with thermal stability in order to characterize the change in the drag coefficient as the surface wind changes direction abruptly over an established wave field.

The Storm Transfer and Response Experiment (STREX) (Fleagle *et al.*, 1982) provided an opportunity to calculate the drag coefficient from aircraft gust probe measurements coincidentally with wave spectral measurements and measurements of atmospheric stability. These measurements allowed the calculation of the magnitude of the drag coefficient

and a parameterization of the effect of sea state on the drag coefficient.

1.1 Interaction between turbulent boundary layer and the underlying surface

The most interesting characteristics of the interaction between the surface layer and the underlying surface are the vertical turbulent fluxes of momentum, τ, heat, q_θ, and water vapor, W_e, on the air side of the boundary. In our investigation of the momentum flux, τ, we can represent the momentum flux as:

$$\tau = - \rho \overline{u'w'}$$

where u' and w' are the longitudinal and vertical components of wind velocity fluctuations, ρ is the air density. τ characterizes the total flux of momentum intersecting the underlying surface in almost the entire thickness of the boundary layer.

The most frequently sought formulation of the small-scale interaction between the atmospheric surface layer and the underlying surface reduces to a determination of these fluxes by means of an external, readily measured variable, such as:

$$\delta U = U_a - U_w \cong U_a$$

where subscript a represents standard height measurement in the atmosphere, for example 10 meters, and w corresponds to the surface measurement, *i.e.*, the speed of the water.

From this quantity, together with density, ρ, we can form a combination that has the dimension of momentum flux $\rho(\delta U)^2=\rho U_a^2$. The ratios of the true turbulent flux τ to the easily measurable combination is called the drag coefficient

$$C_d = \frac{\tau}{\rho U_a^2} \quad .$$

For any selection of measurement height in the layer z_a, the largest contribution to δU is made by the lowest part of the layer. C_d will depend on the characteristics of the turbulent regime in the immediate vicinity of the underlying surface. Therefore, in order to discuss the variability of C_d, we need to know the laws governing vertical turbulent exchange in the surface layer, $z \cong z_a$, and the hydrodynamic properties of the underlying surface, the ocean surface.

The description of the turbulent regime in a temperature-stratified friction layer is based on the Monin-Obukhov similarity theory (Monin and Yaglom, 1965). According to this theory, in the friction layer there can exist a dynamic sublayer, L , within whose limits the influence of density stratification on the turbulent regime can be regarded as small. Moreover, in the region of the dynamic sublayer, where the effects of interaction of the turbulent boundary layer with the underlying surface are not felt, the turbulence structure can be described by similarity theory for a logarithmic boundary layer.

The closeness of the wall or surface can lead to deviations from the similarity regime of developed turbulence in the logarithmic boundary layer. Also, we can expect to see departures from the log pro-

files of U(z) when measurements are made close to wave height on the sea surface. Hasse *et al.* (1977) found such evidence in measurements made within one wave height of the surface in the tropical Atlantic.

The similarity regime within the dynamic sublayer, L, with a characteristic logarithmic profile, U(z), will be found at heights Z which are much larger than:

h_s = the characteristic height of the roughness elements

and

δ_v = the thickness of the viscous sublayer.

The complete group of dimensionless parameters governing C_d could then be expressed as:

$$C_d = C_d \left(\frac{z}{h_s}, \frac{z}{L}, \frac{h_s}{\delta_v}\right)$$

L, the Obukhov length scale has, in the temperature stratified case, the form

$$L = - \frac{C_p \rho \theta_v u_*^3}{kgq_\theta}$$

where g is gravitational acceleration, θ_v is the average virtual potential temperature in the surface layer, $u_* = \sqrt{\tau/\rho}$ is the friction velocity, and $k \sim 0.4$ the von Karman constant.

The ratio $z/_L$ is related to the Richardson number

$$R_i = \frac{g d\theta/dz}{\theta (du/dz)^2}$$

which characterizes stability in the temperature-stratified surface layer.

We can then write

$$C_d = C_d \left(\frac{z}{h_s}, R_i, Re_s\right)$$

where Re_s is the roughness Reynolds number. In general then C_d depends on three dimensionless parameters.

We can use the work of Businger and Dyer as a basis for calculating the effect of stability on the drag coefficient and by compensating for stability, effectively calculate the drag coefficient for a neutral atmosphere, C_{dn}. Then

$$C_{dn} = C_{dn} \left(\frac{z}{h_s}, Re_s\right)$$

The functional form of $f(Re_s)$ has been the object of several investigations (Kitaigorodskii, 1968; Kondo *et al.*, 1973; SethuRaman and Raynor, 1975). Basically, the roughness regime breaks down into three areas. The first, aerodynamically smooth flow is scaled by δ_v is determined by parameters ν, the kinematic viscousity of air and u_* such that

$$\delta_v = \nu/u_*$$

The expression for Re_s then is

$$Re_s = \frac{h_s u_*}{\nu}$$

If the underlying surface is homogeneous and reasonably steep but with vertical dimensions still smaller than the depth of the sublayer, *i.e.*, $h_s \ll L$, then for large values of Re_s the main resistance to the flow will come from the normal pressure on the roughness elements. In this case, the drag coefficient has to be independent of the air viscosity, ν, and therefore

$$f(Re_s) \sim \text{constant}$$

and

$$z_o \sim h_s$$

Conversely when $Re_s \ll 1$, the drag will depend on ν and be independent of the scale of the underlying roughness. Then

$$f(Re_s) \sim \frac{1}{Re_s}$$

and

$$z_o \sim \delta_\nu$$

For an incompletely rough surface, there must be a transition zone between the two cases. Numerous studies have been made in an effort to determine the form of the function $f(Re_s)$ for a range of Re_s. Nikuradse's classic studies (1933) are often quoted as a basis for development of the limiting-drag regimes for immobile boundaries. An adequate representation of aerodynamic roughness has been sought exten-

sively in the oceanographic literature (Kraus, 1966; Kondo, 1975; SethuRamen, 1978).

Most studies of smooth flow or aerodynamically incomplete roughness use wave tanks or short-fetch-limited regimes. Our investigation will deal only with field data and completely rough regimes.

Therefore, we can treat Re_s as a constant and

$$C_{dn} = C_{dn}\left(\frac{z}{h_s}\right) \quad .$$

utilizing the formulas of logarithmic boundary layer theory for the neutral case.

$$du(z) = \frac{u_*}{k}\,\frac{dz}{z}$$

integrating

$$u(z) = \frac{u_*}{k}\,\ln\left(\frac{z}{z_o}\right)$$

where z_o is the integration constant.

Remembering that

$$C_{dn} \equiv \frac{\tau}{\rho U^2} = \frac{\tau}{\rho u_*^2\left[\frac{1}{k}\ln\frac{z}{z_o}\right]^2}$$

and

$$u_*^2 = \frac{\tau}{\rho}$$

we have

$$C_{dn} = \left[\frac{1}{k}\ln\frac{z}{z_o}\right]^{-2}$$

Within the limits of the surface layer, C_{dn} will depend only weakly on z. The only unknown, therefore, is z_o. However, z_o is very difficult to measure on the ocean surface, and usually it is inferred from atmospheric wind profile measurements when they are available, or assumed a constant or derived from a model. As a result, previous work which deals with finding a momentum drag coefficient necessary for relating bulk measurements to momentum flux has most often been pursued without consideration of the underlying sea state.

Garratt (1977) reviewed all of the available data for calculating drag coefficients, terrestrial and marine, and concluded basically that C_d is a slightly increasing function of wind speed. Smith and Banke (1975), using additonal data ranging from a gentle breeze (7 m/sec) to strong, gale force winds (21 m/sec) found a significant increase in the drag coefficient with wind speed which was well described by the equation of Charnock (1955). Smith and Banke also reviewed some earlier results and concluded that

$$10^3 C_d = 0.63 + 0.066 \bar{U}_{10} \pm 0.23 \text{ with } \bar{U}_{10} \text{ in m s}^{-1}$$

describes all of the results well.

They noted that

$$C_{dn} = k^2 \left[\ln \frac{z}{z_o} \right]^{-2}$$

fits the data as well if

$$z_o = a \frac{u_*^2}{g}$$

with $k = 0.4$ and $a = 1.44 \times 10^{-2}$, which is very close to Charnock's original suggestion of $a = 1.23 \times 10^{-2}$. Later investigations by Smith (1980) show a slightly smaller increase of C_{dn} with wind speed.

$$10^3 C_d = 0.61 + .063 U_{10}$$

for winds from 6 m s^{-1} to 22 m s^{-1}. At U_{10} = 15 m s^{-1}, this value is 11% lower than the composite value of Garratt (1977).

Smith did find an interesting anomaly in his later data sets. The drag coefficients were frequently much lower during alongshore winds than during offshore or onshore winds. A linear regression of C_{10} on $H_{1/3}$ for cases of onshore winds and near-neutral stability was performed by Smith (1980) (Fig. 1.1) who found a slight increase of C_d with wave height, but a lower correlation between wave height and C_d than between wave height and wind speed. Smith concluded that wave height is not as good an indicator of C_d as wind speed. Since wave height is to a large extent dependent on present or past wind speed, it appears that one cannot help but conclude that wave height alone is not a reasonable indicator.

Large and Pond (1981) using measurements made by eddy correlation and dissipation methods on a deep-water tower found that the drag coef-

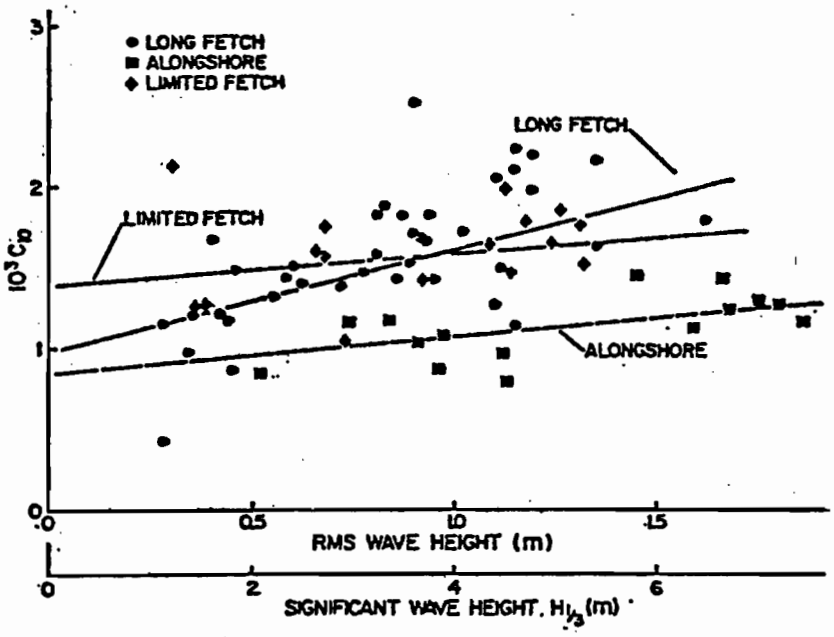

Figure 1.1 Drag coefficients vs. RMS wave height. (*After Smith, 1980.*)

ficients from 196 Reynolds flux measurements agreed well with those of Smith (1980). They found the drag coefficient, reduced to 10-m height and neutral conditions, C_{dn}, is independent of fetch (for fetch/height $\geq$ 800), but that C_{dn} increases with wind speed above 10 m/sec. Some of their time series of C_{dn} will be discussed later in connection with additional sources of variation in C_{dn}.

Several investigators have computed the drag coefficient from profile measurements and found substantial variations in C_d which were virtually uncorrelated with the wind speed. Figure 1.2 shows the drag coefficient as a function of wind speed found by Ruggles (1970) using 299 mean wind profiles. Ruggles termed the region of large variabilities in C_d *discontinuities*, but noted that failure to consider the momentum partition of energy going into wave development left unanswered the question whether the values of C_d are characteristic of a rising, falling, or fully arisen sea. He speculated that the nodes or discontinuities may be a result of differences in physical states of the ocean surface, such as wave-generating conditions as contrasted with nongenerating conditions.

Kitaigorodskii (1970) found that C_d was generally a constant function of wind speed U_{10} to approximately 7 m/sec, where it then showed a tendency to increase. He noted, however, that the concept of critical wind speed for mean values of C_d is rather arbitrary because the differences in mean values of C_d even for large changes in wind speed could be smaller than the differences in values of C_d at different stages of wave development, but the same wind speed. Kitaigorodskii

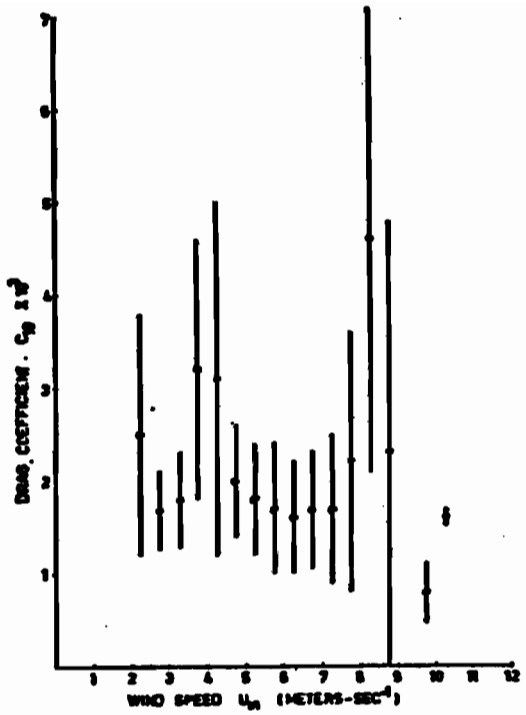

Figure 1.2 Drag coefficients vs. wind speed. The vertical bars show the range of C_{10} measured for the various wind speeds. The large variations were not explained, only noted as discontinuities. (*After Ruggles, 1970.*)

suggested grouping C_d measurements according to values of c_p/u_* where c_p is the phase velocity of the wave with the frequency of the peak of the wave spectrum. Figure 1.3 shows the drag coefficient as a function of c_p/u_* and shows the tendency for C_d to reach a minimum as the wave field ages. His data were limited to wind speed between 4 and 15 m sec. Busch (1977) reported that Hedegaard and Busch analyzed velocity profiles measured on a tower in 25 meters of water in the Kattegat and found

$$10^3 C_d = 0.64 + 0.14\ U_{10} \pm 0.29$$

corresponding to a = .217 in Charnock's relationship with k = 0.35. This seems to be high in relation to other results, but the measurements were made with an unobstructed fetch of 135 km, no swell, and relatively shallow water, all of which can contribute to a wave field that would differ from those of previous investigations.

Denman and Miyake (1973) observed that drag coefficients tended to increase on the leading side of a storm. They estimated that the drag coefficient was dependent on the nature of the wave field to the order of 20%. Similarly, Large and Pond (1981) found situations with frontal passages where the drag coefficient at a given wind speed was twice as large behind the front as ahead of it. Figure 1.4 shows a frontal passage at the Bedford Tower (Large and Pond, 1980). Consider the two measurements at hour 2 and hour 32 in Figure 1.4. Although the wind speeds are about the same (7 m/sec^{-1}), the stress estimates differ by a factor of 2. Large and Pond felt that a greater surface roughness z_o

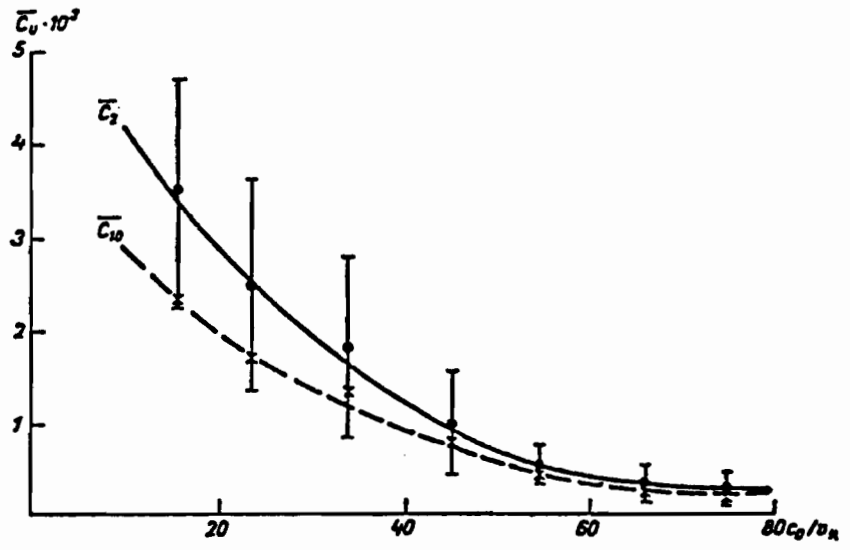

Figure 1.3 Drag coefficient C_d as a function of the dimensionless parameter c_o/u_*. (*After Kitaigorodskii, 1973.*)

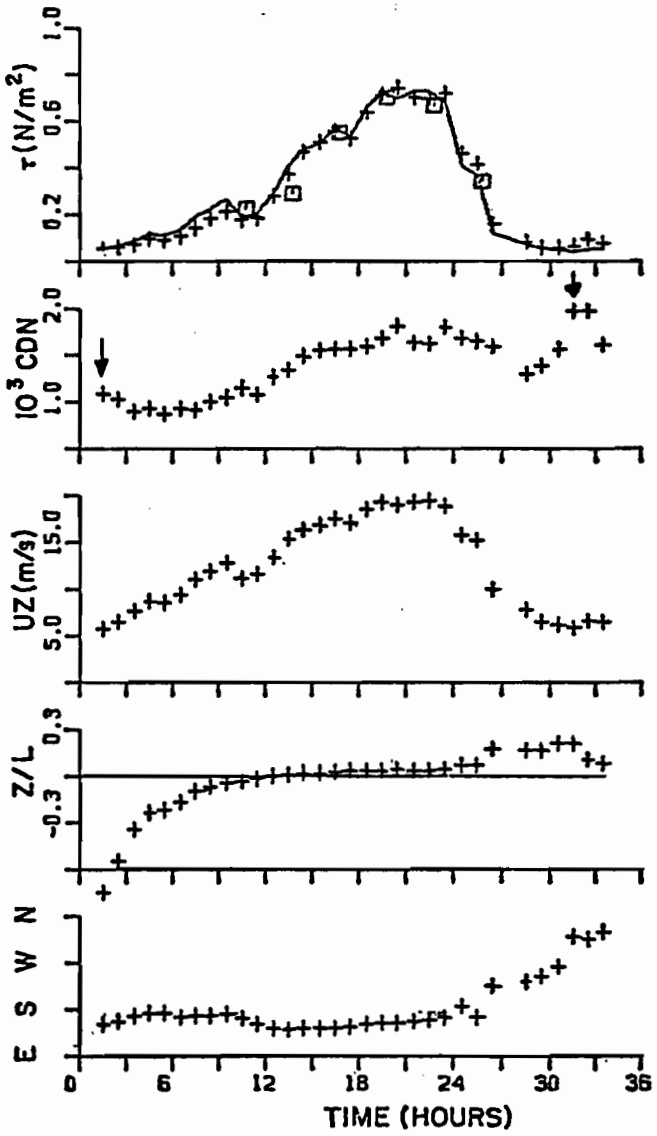

Figure 1.4 Time series from 0440 GMT 7 December 1976. Momentum fluxes are from the dissipation (pluses), Reynolds flux (squares) and bulk (solid line) methods. (*After Large and Pond, 1981.*)

at hour 32 due to the shift in winds produced a larger stress and shear but the same U_{10}. Large and Pond did not make any wave measurements to accompany their atmospheric data. Krugermeyer *et al.* (1978) reported that the dimensionless profile slope, when measured from a mast on a surface-following buoy, increased with wave height almost three times faster than the drag coefficients found by Smith. This result casts some question on relationships of C_d vs U_{10} based on wind profiles but should not affect eddy correlation measurements.

Donelan (1977), using data from the Great Lakes, proposed a wind-coupling model in which the wind drag induced by each component of the wave field is proportional to the slope of the component and the square of difference of the phase velocity of the peak frequency wave and the wind speed. However, the model produced extreme values of C_d under oceanic conditions. It was, however, one of the first utilizations of wave height and peak frequency in an attempt to predict C_d.

Hsu (1974) made an effort to include wave height in a representation of z_o and found $z_o = (2\pi)^{-1}\xi\ (c/u_*)^{-2}$ where ξ is the wave height. Hsu's values of z_o systematically underestimated the drag coefficient for the 15 November warm sector data by $\sim$ 23%.

There is a serious defect in all of the techniques examined above, one which may stem from the geographical location of the investigators original data set. In enclosed seas such as the North Sea, the JONSWAP location, or the Great Lakes, the wave spectral peak usually reflects the energy in the wind sea, and the wind sea either dominates or is quite distinct from the swell field. However, in the open ocean, for example, the northeast Pacific, the wave spectra usually look like

Figure 1.5 taken by the National Data Buoy #42-02. When there is an abrupt change in wind direction, however, such as a frontal passage (Fig. 1.6), the spectra still retain a dominant swell peak. Therefore, the spectral peak frequency cannot be used to characterize the wave field except where there are high winds for long periods of time for example, and where the total wave field is changed into a wind sea and where, in fact, the constant high winds are the source of the pervasive 12- to 14-sec swell.

We see that there has been a great deal of work relating C_d to surface wind speed and, in some cases, to qualitative evaluation of the wave field. However, the wave analysis has been limited to $H_{1/3}$ representations of wave height and peak frequency of wave spectra in select regions. Hasselmann (1976) has shown under certain equilibrium conditions wave spectra can be parameterized by two variables--amplitude and peak frequency. This parameterization limits the calculation of the roughness length to a single length scale and a related wave speed, which is tightly coupled to U_{10}.

It is the hypothesis of this study that sea state has an effect on roughness length and C_d that cannot be accounted for as merely a function of wind speed. The complicated processes of surface wave generation must be included in determining C_d. It appears that there are conflicting theories and conflicting data sets. There is little doubt that in order to properly account for the scatter and variation of C_d, the surface wave characteristics must be included more comprehensively than previously. We can represent the response of the wave field to the

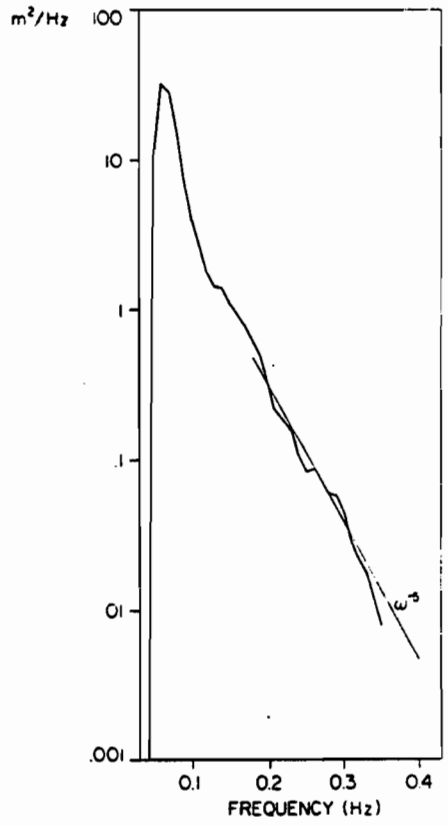

Figure 1.5 NDBO #42-02 equilibrium wave spectrum.

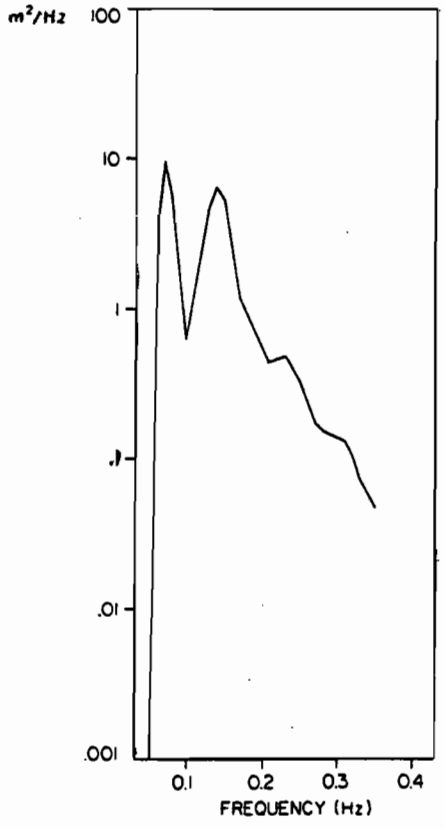

Figure 1.6 NDBO #42-02 wave spectrum.

atmospheric input by analyzing the complete wave spectrum, rather than just $H_{1/3}$ and the peak frequency.

The drag coefficient is apparently very sensitive to surface wind speed, phase speed of the waves in the surface spectrum, and spectral distribution of the surface wave energy. We have seen that C_{dn} can be expressed as a function of only z_o. Therefore, it would suffice to know a single parameter, z_o. The basic parameter z_o would assume an elementary form that returns the basic parameterization derived earlier. Therefore, we have

$$z_o \alpha h_s$$

where h_s is a characteristic scale of the surface roughness elements.

1.2 Classification of the underlying surface

Because the neutral surface layer has a logarithmic wind profile given by

$$U(z) = \frac{u_*}{k} \ln z/z_o$$

the only parameter that is related to sea state is z_o. z_o is the scale length of the roughness that is felt by the flow. Actual determination of z_o over the ocean covers a wind range of values (Roll, 1965).

Two sets of determinations of z_o done by Kraus (1967) are shown in Figure 1.7. Buzzards Bay on Cape Cod, Massachusetts, is an enclosed area with often-confused wave patterns. Near Aruba, an island in the eastern Carribean, a fairly regular wave pattern is developed in steady offshore winds. C_d calculated from these values of z_o were found to be

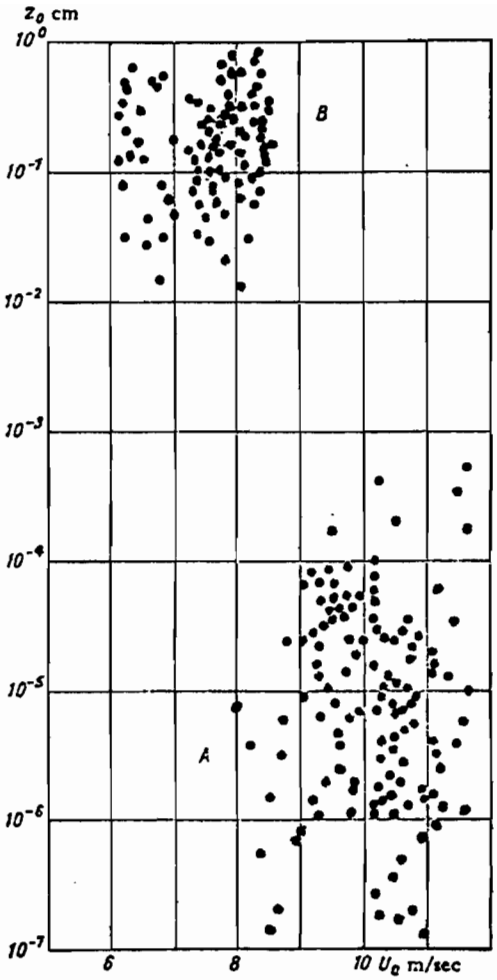

Figure 1.7 Roughness parameter z_o as a function of wind speed U_{10}. A--results obtained in Buzzards Bay for extremely irregular waves (short fetches): B--results obtained for developed wind waves during stable trade winds. The same equipment was used during both observations. (*After Kraus, 1967.*)

100% higher in the Buzzards Bay measurements than in the Aruba measurements, although the wind speed, U_{10}, in the latter region was generally higher.

Figure 1.8 shows a compilation by Kitaigorodskii of roughness parameter z_o as a function of u_* for a large group of different hydrometeorological situations. The figure also includes some empirical relationships for $z_o(u_*)$ proposed by a number of scientists. Data on z_o were used from the works of Gontarev (1975), Bogorodskii (1964), Fleagle, Deardorff, and Badgley (1958), Deacon, Sheppard, and Webb (1956), and others.

Figure 1.8 is shown for several purposes. First, it exhibits the apparent variation of z_o, 10^{-5} m to 10^{-1} m.

Second, the scatter of z_o for a given u_* is large and apparently random. Kitaigorodskii (1973) found the scatter particularly large when comparing results of different scientists.

Figures 1.7 and 1.8 show that the absence of a single-valued relationship between z_o and u_* may be due to the variability of the wave characteristics that affect the drag. These characteristics are not in single-valued relationship with the local wind, but depend on the history of the wind speed and direction and the fetch available for development of the wave field. Wave development has, therefore, a significant effect upon the drag that the sea exerts on the wind. Wave growth continues until waves reach the speed of the wind above the immediate surface. Moreover, the wave energy and momentum increase pass through a maximum before that stage is reached.

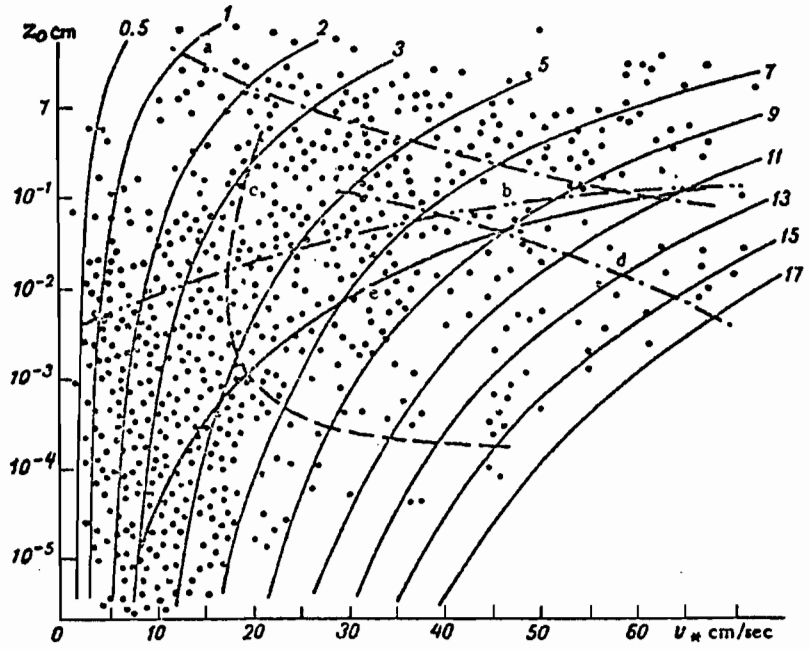

Figure 1.8 Roughness parameter z_o as a function of u_* friction velocity: a--according to Francis (1953); b--according to Neuman (1956); c--according to Goptarev (1957); e--according to Kuznetsov (1963). The fine lines correspond to the logarithmic law governing the mean wind speed profile (this mean wind speed (m/sec) at an altitude of 1 m is indicated by the figure at the head of each curve). (*After Kitaigorodskii, 1973*).

The question then is whether the rate of work of the wind also reaches a maximum. Does the sea surface exert less drag on a wind that has been blowing for a long time or over a long distance? And if there is a variation, what mechanism could be responsible for it?

Previous studies of marine drag coefficient have either neglected the wave field completely or used measurements of only the height of the dominant waves. Characterizing the wave field with only one length scale, height, severely limits the ability to model z_o because the effective density of physical elements of height scale h_s cannot be represented. Similarly, using the height of only the significant wave to calculate marine boundary layer values of z_o neglects the additional possibility that waves that are shorter than those of the peak frequency influence the effective scale of z_o.

Examination of the relationship of the complete spectral energy distribution of the wave field to the calculation of z_o will enable us to account for the contribution of waves that are not at the spectral peak to the surface roughness felt by the marine boundary layer.

We will investigate this problem using stress measurements made with an aircraft gust-probe system and coincident wave spectral measurements from an airborne laser profilometer.

Chapter 2 describes two STREX flights that produced cases pertinent to the investigation.

Chapter 3 describes the data reduction processes used to convert the gust-probe measurements to stress, the normalization of the aircraft flight level meteorological measurements to account for the atmospheric instability, and the laser measurements to surface wave spectra.

Chapter 4 describes the results of the measurements and show the relationships of changes in the wave spectral signature to the changes in the drag coefficient C_d.

Chapter 5 discusses the relationship of the wave spectra to calculation of z_o and shows that in the equilibrium wave fields the representation of z_o tends to Charnock's equation.

Finally, Chapter 6 presents conclusions based on the results of the investigation.

2. CHAPTER II: EXPERIMENT DESCRIPTION

2.1 STREX: Overview

The Storm Transfer Response Experiment (Fleagle *et al.*, 1979) was conceived as a means to study the energetics of mature extratropical cyclones in the north Pacific where energy is exchanged across the boundary layer. Information on this energy exchange is often generated using mean meteorological measurements, (*e.g.*, average velocity, average temperature) and the corresponding bulk transfer equation.

STREX was a multiship, multiaircraft program designed to synoptically measure a series of storms that passed through the Gulf of Alaska between 1 November 1980 and 15 December 1980. Two aircraft were equipped to make boundary layer measurements--the NOAA WP-3D and the NCAR Electra. The NOAA WP-3D carried a laser wave-profilometer system for wave studies, in addition to a complete gust-probe system for measuring turbulent exchange at aircraft altitudes. During seven of the nine flights made by the WP-3D (or P-3), concurrent wave spectral measurements and turbulence transfer measurements were made.

The resulting measurements covered several areas of interest in terms of duration-limited versus fetch-limited wave generation. Some situations of extreme uniformity were sampled with high resolution in an effort to detect subsynoptic-scale motions.

We concentrate on the relation of the change in the surface wave spectral signature to the drag coefficient or momentum exchange over the ocean in measurements taken during two of the flights--the 7 Novem-

ber flight, which was a very stable situation 96 hours after passage of a front, and the November 15 flight through a very strong front with high winds and seas.

2.2 Observation Systems

2.2.1 Waverider

Output from a Datawell waverider buoy, deployed during the experiment at location P′ approximately 300 km east of weather station P, was telemetered via radio to the nearby NOAA research vessel *Oceanographer*, which was to stay close to P′ for the duration of the experiment because of the limited radio range of the buoy, and the lack of station keeping by the *Oceanographer*. Also, there were few complete wave records. During the events of primary interest, the passage of the 15 November front over P′, the *Oceanographer* was out of radio range of the buoy. The resulting wave records are incomplete, and it is impossible to recover a spectrum from them.

2.2.2 Laser Profilometer

The laser wave-profilometer system consisted of a geodetic laser mounted vertically with the laser beam passing through an opening in the belly of the aircraft. The laser was amplitude modulated at 50 Mhz, and the reflection from the ocean surface was phase locked and compared with a reference signal in the originating body. The output from the laser head was integrated for 50 m^{-1} sec and then sampled by an analog-to-digital converter. The system had several values of full-scale reading, *i.e.*, 10, 20, 100, and 1000 ft, but during the experiment the 20-ft scale was used exclusively. The choice of scale determines the maximum altitude variation that the laser will measure

before a phase shift occurs. If the laser signal changes by more than the scale value, the output merely "rolls over" and starts again at zero. This maintains the continuity of the data, but greatly complicates the data processing.

The analog output was digitized at 40 Hz by the aircraft data-acquisition system and stored on the "fast tape" together with other inertial and meteorological parameters measured aboard the aircraft.

The vertical resolution of the laser system is on the order of ±.1 cm, the horizontal resolution is a function of the aircraft ground speed and data acquisition rate and will be dealt with later.

2.3 Description of Experiment Area, Synoptic Weather Conditions, and Measurements Made

2.3.1 Synoptic Description

The field phase of STREX, between 1 November and 15 December 1980, took place over the eastern North Pacific Ocean and used personnel and resources from a variety of organizations in the United States and Canada.

For the period from 1200Z 6 November through 1200Z 13 December 1980, the following meteorological maps were produced:

Surface analysis at 0000z and 1200Z

500-mb analysis at 1200Z

500-mb analysis at 0000Z on mission days only

The procedures for producing these analyses were as follows:

The surface analyses and machine-plotted unanalyzed charts. Any ship reports received over the West Coast Marine teletype circuit and not already appearing on the charts were plotted by hand. STREX drifting-buoy reports were not used in the analysis due to the unreliability of the data in their unedited form. Isobaric and frontal analyses were then made by Prof. R. J. Reed and Mr. S. L. Mullen of the Department of Atmospheric Sciences, University of Washington. Special attention was given to ensuring time continuity, and extensive use of satellite data was made.

A complete meteorological data atlas is available for the experiment (STREX, 1981a).

The following description of flight days provide the synoptic perspective for the wave and wind stress measurements.

November 7, 1980

There was a frontal passage at Ocean Station P at 1200Z on 6 November 1981. When the low-pressure center reached the coast, a secondary low formed at the sea surface. When the secondary low reached the coast ninety-six hours after the frontal passage, the mission was flown.

The flight was designed to study mesoscale air/sea interaction in a well-stabilized, post-frontal regime. (Figure 2.1 shows the weather flight summary and the schematic flight path of the NOAA P-3.) The crosswind/upwind legs, flown at 50-m altitude, were specifically set to investigate the mesoscale variability well behind the front. The laser wave-spectral measurements were made during the upwind leg; the obser-

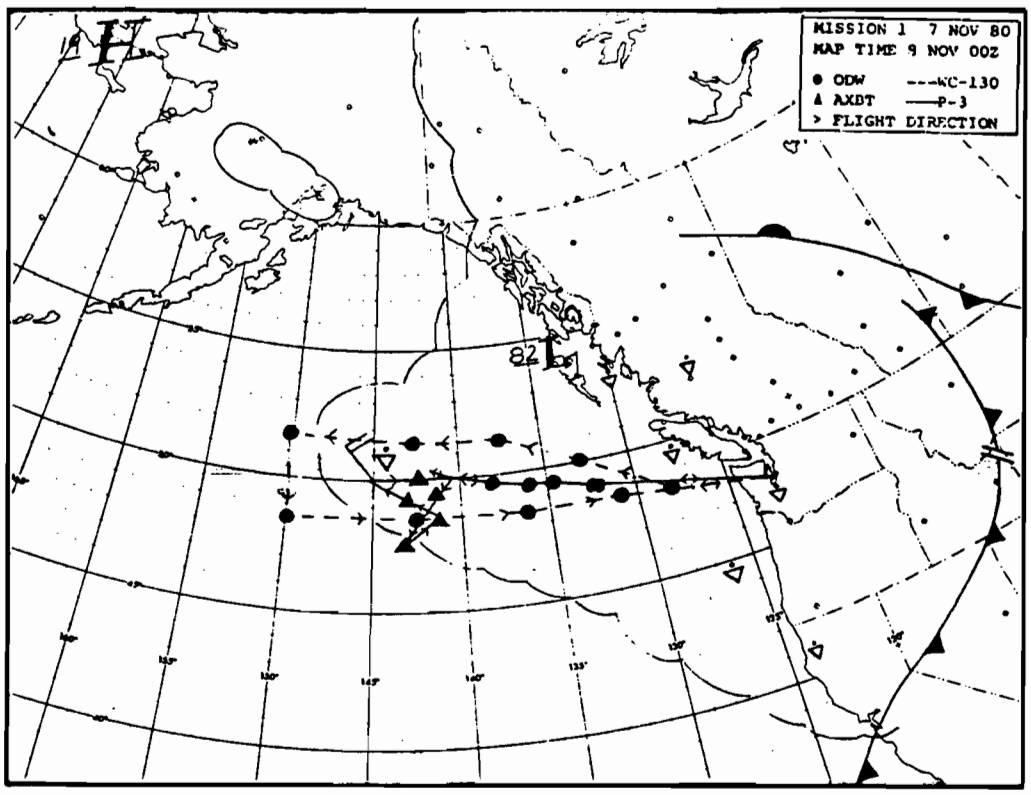

Figure 2.1 Weather and flight track summary 7 November 1980.

vations were made during a period chosen to be as nearly homogeneous spatially as could be found. The upwind leg was flown directly toward weather station P where surface observations showed a steady wind from 320-330° at 10-13 m s^{-1}. The surface wavefield at P was dominated by a 9- to 10-sec wind sea with heights of 3-5 m. The air-sea temperature difference at P was ∿ 2°C unstable.

November 15, 1980

November 15 was a frontal-investigation mission based on the forecast made the previous day. The forecast was borne out with surface observations at the *Oceanographer* of 30 m s^{-1} winds from the south in the warm sector and 15 m s^{-1} winds from the west behind the front.

Surface observations at the *Oceanographer* ahead of the front showed the wind direction primarily from the south with winds gradually increasing until the frontal passage between 1800 and 1900Z. The surface wavefield at the *Oceanographer* was characterized by a 5- to 6-sec wind sea of gradually increasing height reaching a maximum of ∿3 meters at the time of the frontal passage. The swell field preceding the frontal passage between 1800 and 1900Z was out of the south at 180°.

The swell field persisted from the south for an additional 10 hours after the wind changed. By 0400 on the 16th of November, the swell field had come around to 240°, but 24 hours after the passage it came from 270°. The air-sea temperature difference at the *Oceanographer* was 3°C stable ahead of the front and 3 to 3.5°C unstable behind the front.

The front passed weather station P between 0300 and 0600Z with the wind rotating from 170° to 340°. Surface swell observations at P showed the prevailing swell to be from 260°.

From 1800Z on the 15th November to 0000 on the 17th, ocean station P was reporting two swell systems, one from 270°-280° and a second swell system from 150°-160°.

The NOAA P-3 and the NCAR Electra took flight level data in "L" and stair-step patterns. The P-3 passed through the front near the surface at an altitude of 300 m on the westbound passage and at an altitude of 1000 m on the return. The weather and flight track summary of 15 November 1980 is shown in Figure 2.2.

In the analysis of the quality of flight level data undertaken for both the P-3 and the Electra, for both aircraft, winds measured at the end of an "L" were quite consistent. That is, when the aircraft's heading was turned through 180°, the wind velocities and direction remained essentially the same. During the comparison run, the Electra measured an air temperature an average of 0.6°C lower than the P-3. The dewpoint temperature recorded by the P-3 was generally below that recorded by the Electra, although this difference was neither as pronounced nor as consistent as the difference in air temperature. Wind velocities and directions measured by the two aircraft agreed very well.

2.3.2 Satellite Observations of the Experiment Area

Both the GOES geosynchronous satellite images and the NOAA-6 polar orbiter provide visible cloud images as well as thermal infrared images

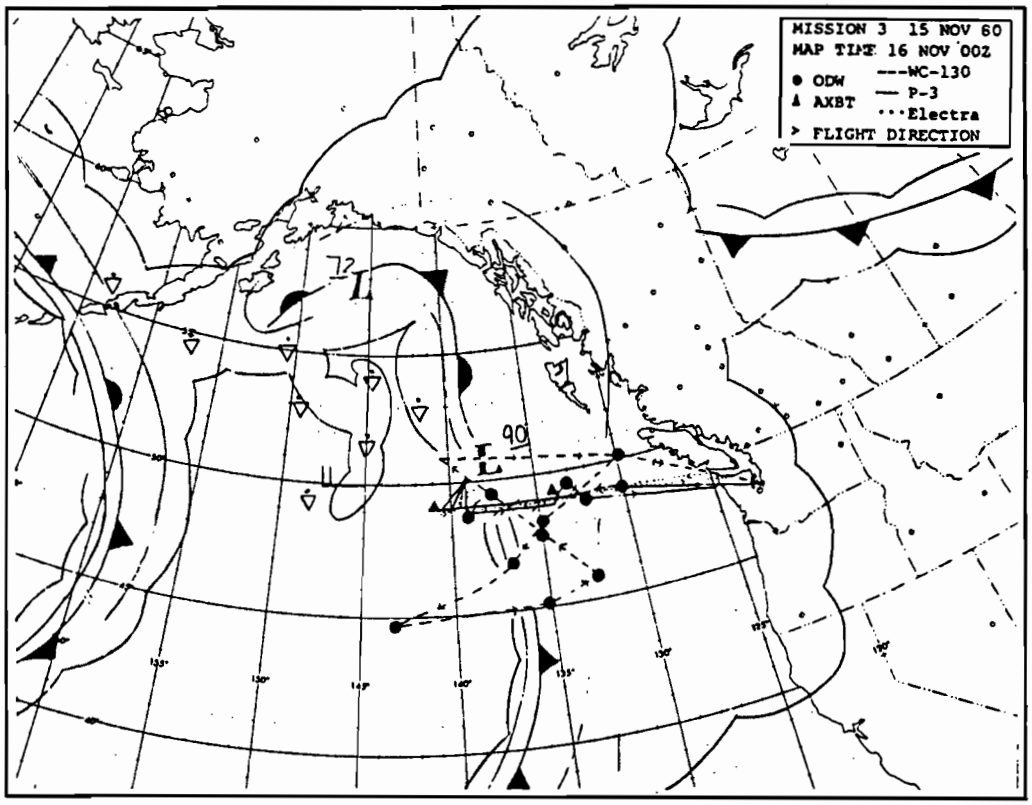

Figure 2.2 Weather and flight track summary 15 November 1980.

for 7 November and 15 November. The 7 November images show the previously mentioned stationary postfrontal regime. The 15 November sequence shows high clouds overlying the cold front that seems to lag behind the position of the front as calculated from aircraft data. This discrepancy may be a result of inexact registration of the geosynchronous images.

The 15 November sequence does show the motion of the front and the unstable regime in the cold sector, and the position of the low to the north of the flight region and the curvature of the front as one moves northward are also apparent. The curvature and subsequent wrap-up of the storm about the low caused the front to translate eastward more slowly in the more northern areas. This may explain why the speed of advance of the front was somewhat slower at the *Oceanographer* at 50°N than in the area of the aircraft operation at 49°N.

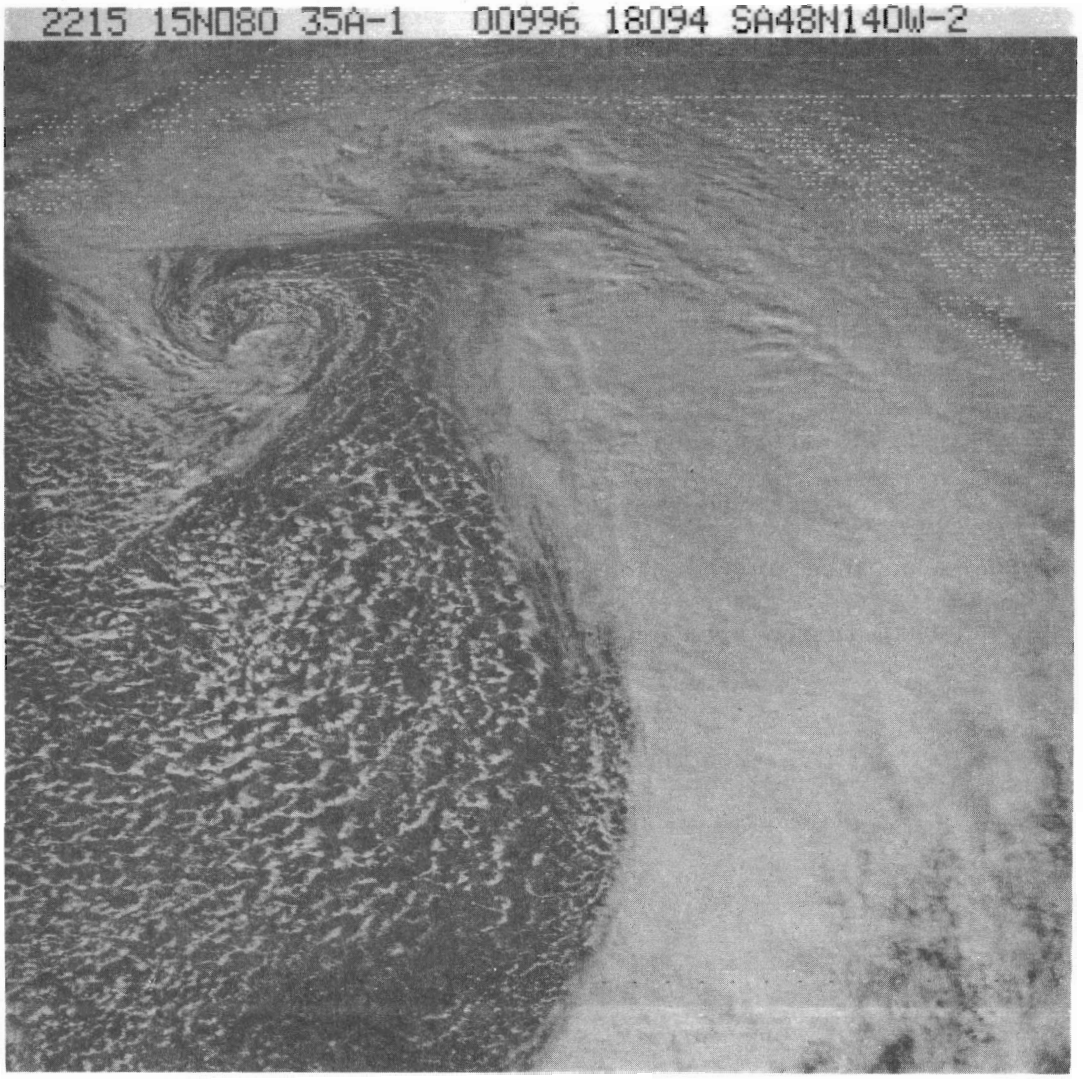

Figure 2.3 Geosynchronous satellite picture of 2215, 15 November 1980.

Figure 2.4 Geosynchronous satellite picture of 0015, 16 November 1980.

3. CHAPTER III: DATA REDUCTION

3.1 Wave Data

The earliest attempt to observe waves directly from low-flying aircraft involved the use of sensitive radar altimeters (Lonquet-Higgins *et al.*, 1963; Barnett and Wilkerson, 1967) to obtain a profile of the surface waves. Wave heights and periods were measured during STREX using an airborne laser system.

Both radar and laser systems have been used previously in fetch-limited wave growth studies. Data obtained by Ross *et al.* (1970), Ross and Cardone (1974), and Barnett and Wilkerson (1967) are shown plotted as a function of nondimensional fetch as suggested by Kitaigorodskii (1973) in Figure 3.1. Results from all fetch-limited studies follow the general developmental properties described in Hasselmann *et al.* (1973).

The laser output is sampled at 40 Hz and recorded on digital magnetic tape. Calibration for the data is provided by latching the laser output at its maximum and minimum value and recording the digitized output. The laser experiences phase-shifts or "rollover" if the aircraft motion or wave heights exceeds the scale set in the laser instruments. During STREX, the laser profilometer was uniformly set at 6-m scale, and the resulting phase-shifts were removed during the digital processing of the data.

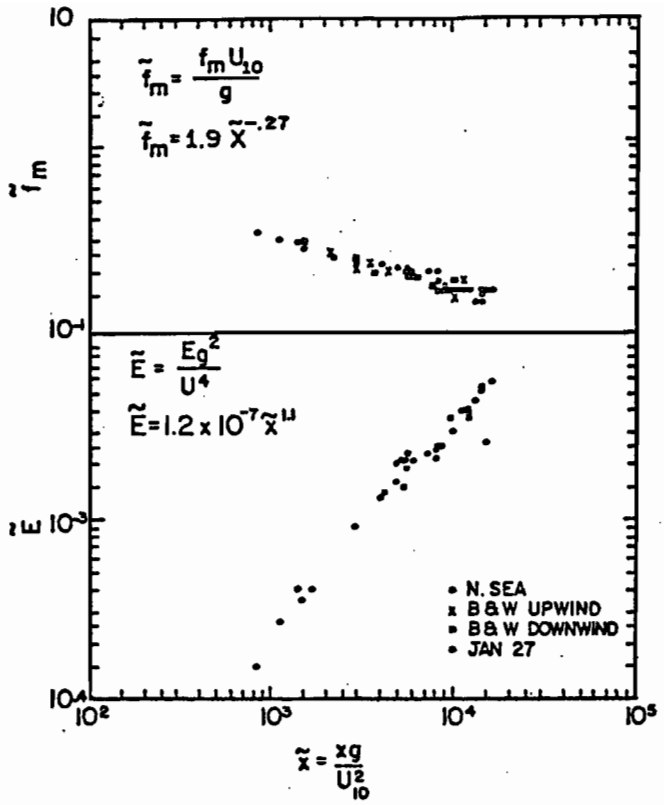

Figure 3.1 Observations of the fetch ($\tilde{X}$) dependence of the total energy ($\tilde{E}$) (twice the variance) and spectral peak frequency ($\tilde{f}_m$) nondimensionalized by the surface wind as measured at 10 meters, and gravity. The closed and open circles are the data of Ross *et al.* (1970) and Ross and Cardone (1974); the crosses and boxes are the data of Barnett and Wilkerson (1967). (*After Ross, 1977.*)

3.1.1 Computer Processing

The data from the laser system was processed on a Digital Equipment Corporation PDP-11/55 computer. Processing required reading raw data from magnetic tapes generated on board the aircraft by the Research Flight Center (RFC) at Miami, Florida, editing the data for glitches and phase-shifts, detrending the data for drift, and filtering out aircraft motion. A block diagram of the aircraft laser data processing is shown in Figure 3.2. The format of the data tapes is not simple, but it is straightforward. Each second of data is carried on one record, and the format for the RFC fast tape is available from RFC, Miami.

The segments of data used for the spectral calculations were separated from the ingest tape and stored on random access disk files. A subset of the total number of variables included on the RFC fast tape is usually utilized. Once the disk files have been generated, the work on the data is done interactively from video terminals with intermediate sets of plot output generated to facilitate checking of the data processing. Figure 3.3 shows a plot of the raw laser data as output onto the RFC tape. The laser output must be edited to remove the phase shifts and glitches. The resulting plot of the edited data is shown in Figure 3.4. The resulting data are then detrended and high-pass filtered.

3.1.2 Removal of Aircraft Motion

A principal requirement for use of aircraft profilometers for wave studies is the removal of aircraft motion. Barnett and Wilkerson

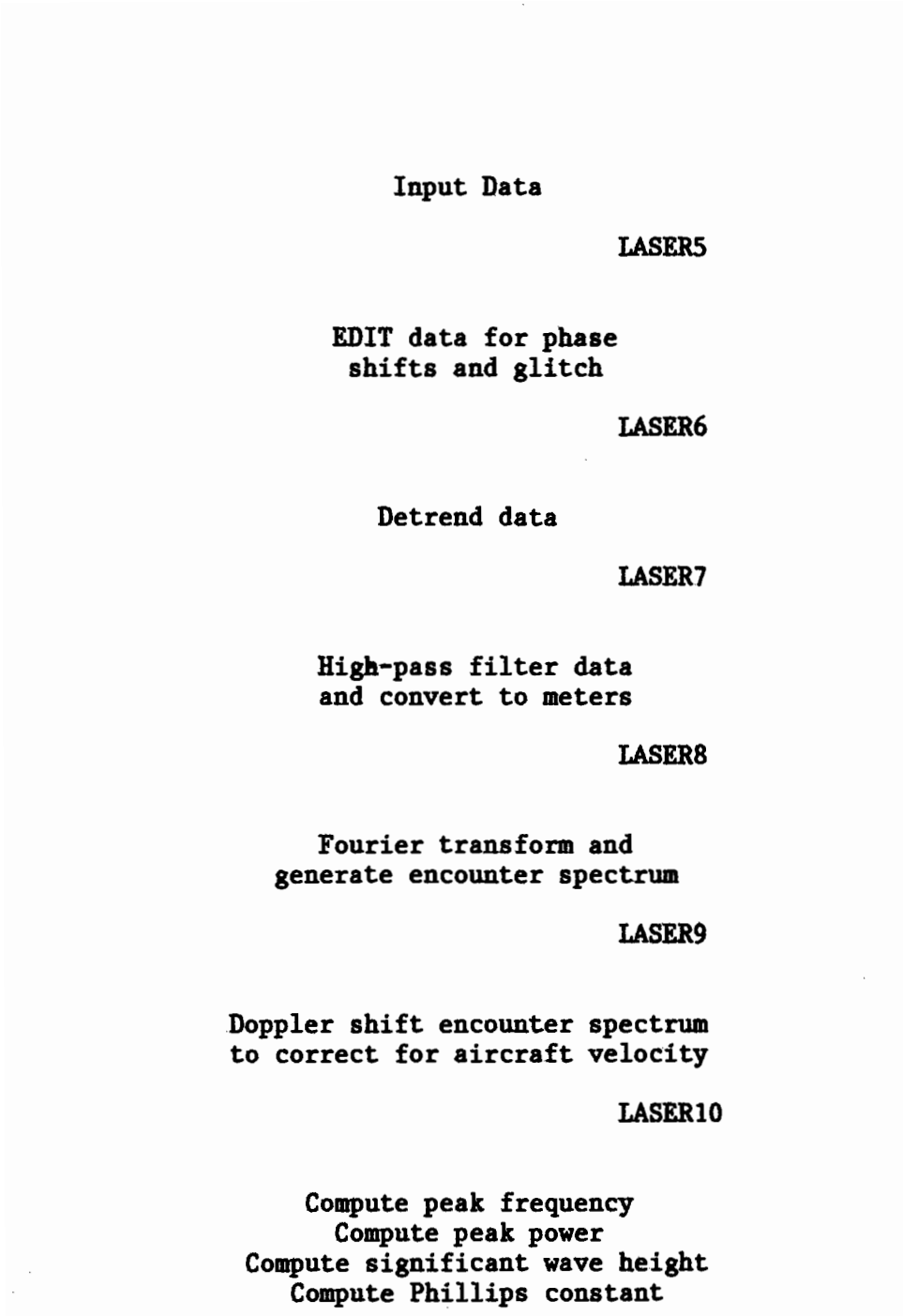

Figure 3.2 Block diagram of aircraft laser data processing.

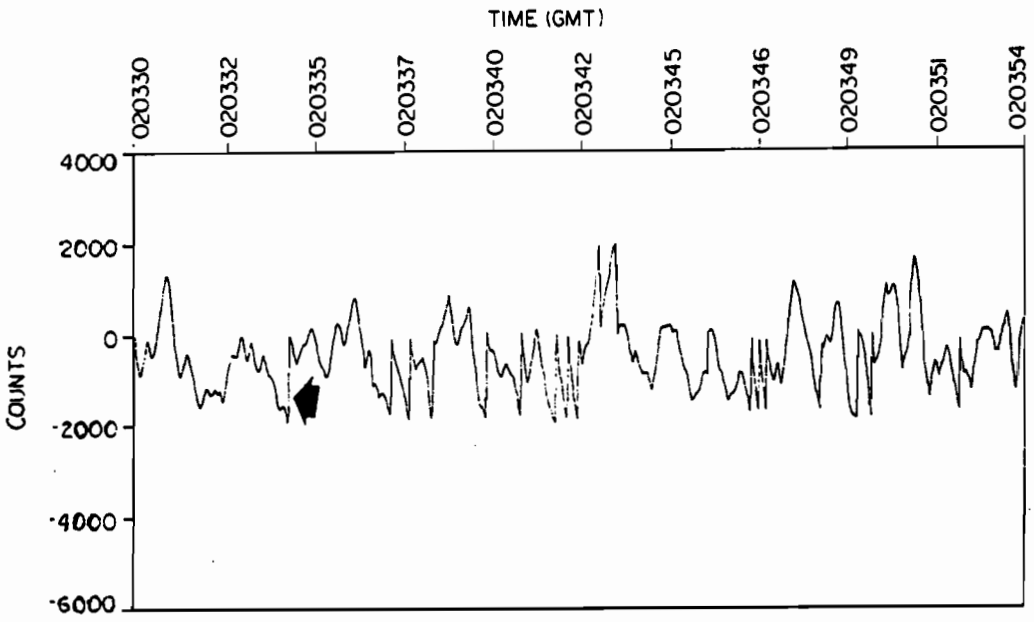

Figure 3.3 Plot of raw airborne laser data from 0203:30 GMT to 0203:54 GMT. The data are shown in units of -2047 to +2048 counts. The raw data are characterized by rollovers (see arrow) which occur when the range of the laser is exceeded by the change in wave height or aircraft altitude. Removal of rollover and calculation of the actual height is performed by LASER6.

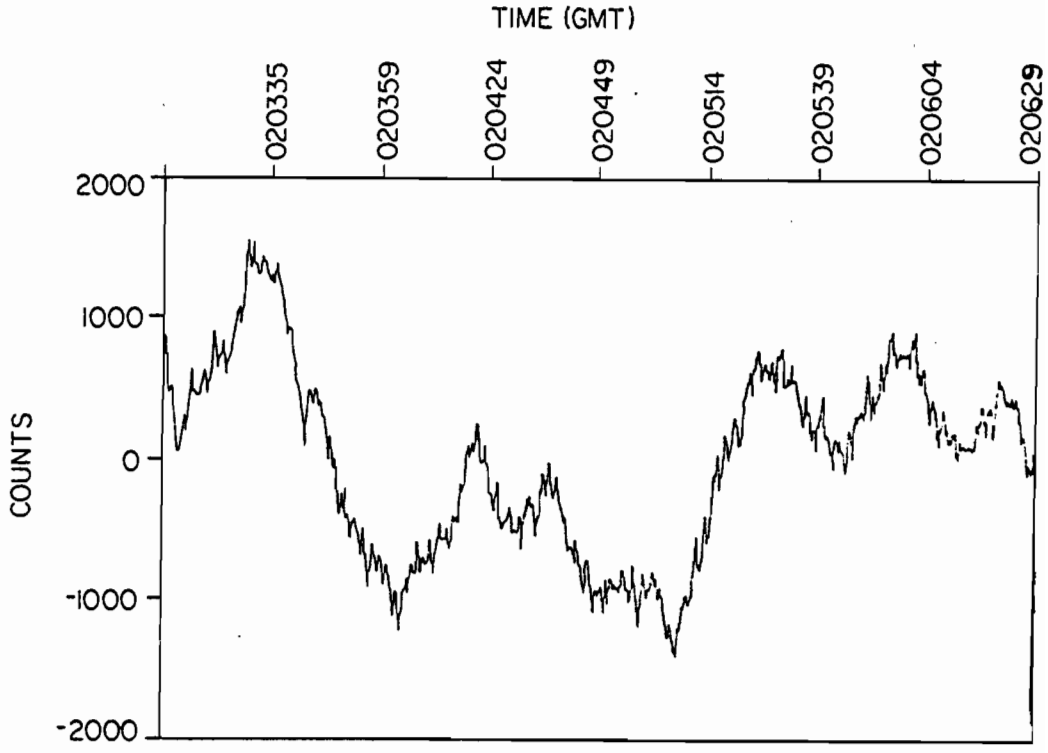

Figure 3.4 Edited airbourne laser data. Note the time scale is much larger than in Figure 3.3. The time covered extends from 020335 GMT to 020629 GMT. Also, note the increase in scale still in units of counts. The large variations which are apparent are the altitude changes due to aircraft motion. The smaller changes are the wave profiles.

(1967) removed aircraft heave displacements by double-integrating and subtracting the output of a vertical accelerometer from the altimeter output. Low-frequency energy remained, however, due to pitch-and-roll errors and was removed by digital high-pass filtering prior to Fourier analysis of the wave time series. Aircraft motion in the STREX laser data was removed by digital high-pass filtering the laser time series. This approach is based upon the assumption of little aircraft motion in the surface wave passband. This assumption is substantiated by the characteristic dip that normally occurs in the unfiltered laser spectrum in the region separating wave energy from aircraft motion (Ross, 1977). Figure 3.5 shows the spectrum from an unfiltered laser time series obtained in Pacific Hurricane Ava in June 1973. Figure 3.6 shows the same spectrum following high-pass filtering of the data. The filter response also plotted on Figure 3.6 shows the energy at the frequency of the dip is 60% passed, the drop at the dip is only 13% of the spectral peak and, therefore, the dip in the spectrum is real.

The data were taken during this study using the identical aircraft and instrument as used by Ross for calculating the spectral response shown in Figures 3.5 and 3.6.

The example wave record is shown in Figure 3.6 after being high-pass filtered. The numerical high-pass filter applied to the laser data was a symmetrical filter with a Lanzcos squared taper. The filter was so constructed that the 6-db downpoint (1/2 amplitude) 1/4 energy occurred at .009 nyquists. In order to generate a sharp filter

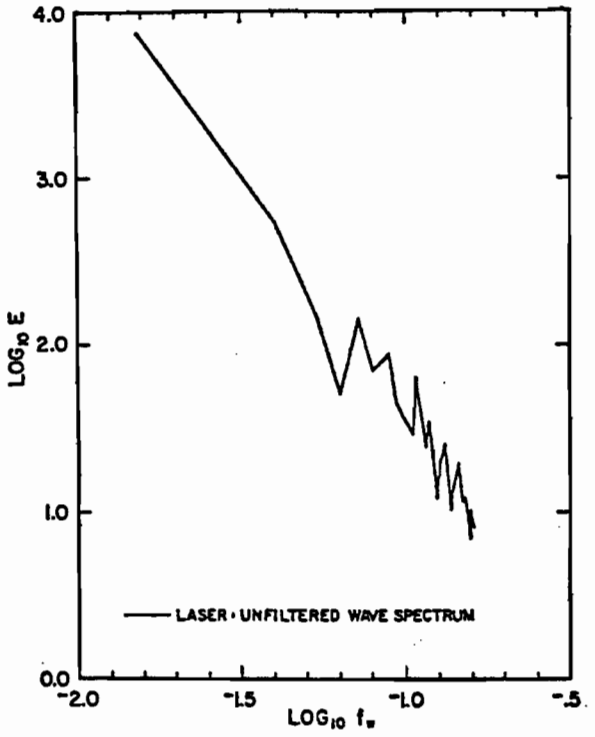

Figure 3.5 Log-log plot of unfiltered laser altimeter spectra showing characteristic dip (at $\log_{10} f_w = -1.2$ or $f_w = .063$ Hz) separating the region of aircraft motion from that of wave energy. The frequency axis shown has been mapped from a moving to a fixed coordinate system. (*After Ross, 1977.*)

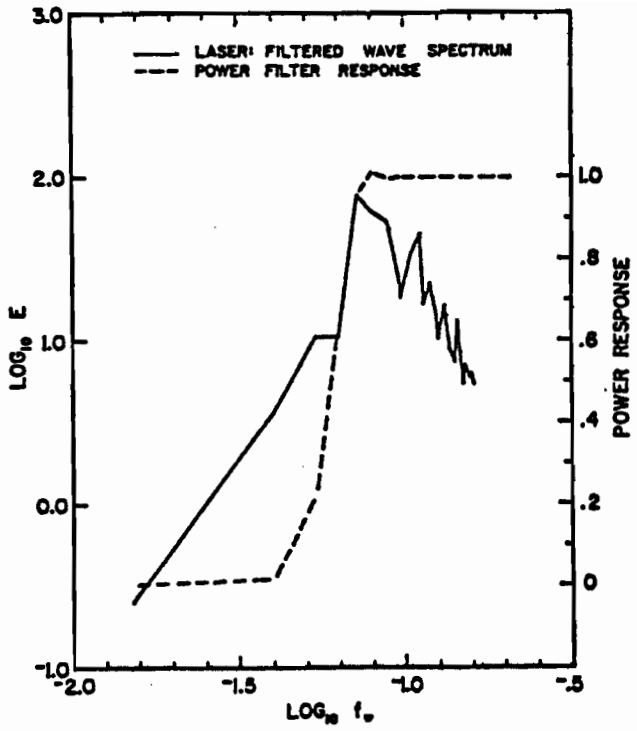

Figure 3.6 Log-log plot of wave energy spectra resulting from high-pass filtering the data used to produce the spectra of Figure 3.5. From the filter response also shown, it can be seen that the power is 60% passed at the frequency of the characteristic dip in Figure 3.5. (*After Ross, 1977.*)

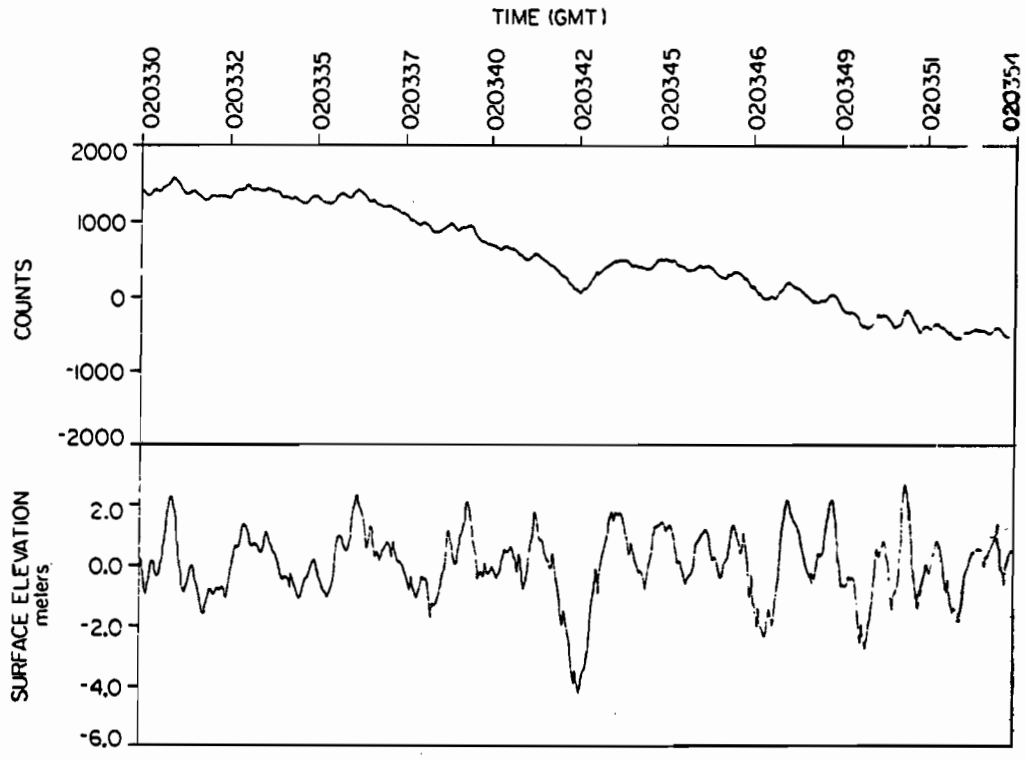

Figure 3.7 *Upper panel:* Plot of the high-pass-filtered laser data shown in Figure 3.3. The data have been detrended using the entire 3-minute record. *Lower panel:* The short segment of the file has been high-pass filtered and converted to meters.

without extensive side lobes, an unusually large kernel was necessary. The filter used required a 400-point kernel to produce a 6-db down point at .009 nyquists.

3.1.3 Spectral Calculation

Spectral analysis of one- or two-dimensional records of sea surface elevation yields one- or two-dimensional encounter spectra, which are actually weighted integrals over the real two-dimensional surface wave spectrum. Long (1979) has examined in detail the problem of translating the moving reference frame to the stationary frame. He has shown that the integral relationships are determined by the type of record and the motion of the observer relative to the water on which the waves are running. An extensive discussion of profilometer wave data is included in Barnett and Wilkerson (1967). To obtain a solution to the integral relations, it is necessary to represent the two-dimensional spectrum as a product of a frequency-dependent function and an angular spreading factor,

$$F(\sigma,\psi) = H(\sigma)K(\sigma,\psi)$$

where σ is the real wave frequency and ψ is the angle between the aircraft velocity and the surface wind.

Since in these experiments the aircraft flight paths were upwind only and aircraft data were our only method of obtaining direct estimates of $K(\sigma,\psi)$, we assumed

$$K(\sigma,\psi) = K(\psi) = \delta(\psi)$$

that is, that all of the waves are traveling in the direction of the wind. Barnett and Wilkerson explored several functional representations of $K(\sigma,\psi)$ and found that the spectral energy representations were not very sensitive to functions which differed from $\delta(\psi)$.

3.1.4 Doppler Correction for Aircraft Motion

The filtered, free-surface height data were then Fourier transformed to generate spectral coefficients in the encounter frame of the moving aircraft. The encounter spectra are doppler shifted from the real wave frequency by the aircraft ground speed and the angle between the aircraft track and the direction of wave propagation.

There exists a unique relationship between the real wave frequency σ, and the apparent wave frequency ω.

$$\omega = \sigma - (\sigma^2 V/g)\cos\psi$$

where V is the speed of the moving platform and ψ is the angle between the direction of platform motion and the direction of wave propagation. However, the inverse relation

$$\sigma = \{1 \pm [1-(4\omega V/g)\cos\psi]^{\frac{1}{2}}\}/[(2V/g)\cos\psi]$$

is not unique. The speed of the platform and the value of ψ determine which branch of the equation is to be considered. Since our aircraft travels much faster than the fastest wave and since we are interested in the wind sea, it is reasonable to assume that all of the energy is

within ± 90° of the mean wind direction. ω then will be negative and it is helpful to rederive ω and σ such that

$$\omega = -\sigma + (V\sigma^2/g)\cos\psi \qquad \psi < \pi/2$$

and

$$\sigma = \frac{\{1 + [(4\omega V/g)\cos\psi]^{\frac{1}{2}}\}}{(2V/g)\cos\psi} \qquad \psi < \pi/2$$

The energy spectrum and distribution is also doppler shifted and must be corrected

$$E_\sigma = E_\omega\,[1 + (4\omega V/g)\cos\psi]^{\frac{1}{2}}$$

An example of a doppler corrected spectrum is shown in Figure 3.8.

3.1.5 Calculation of β

Phillips wave parameter β (Phillips, 1966) was calculated for each of the laser wave spectra. The representation of the wave spectra by Phillips model assumes,

$$S(\omega) = \beta g^2 \omega^{-5} \quad \text{for } \omega > \omega_{max}$$
$$= o \quad \text{for } \omega < \omega_{max}$$

where $S(\omega)$ is the spectral energy density, g is the gravitational constant, and ω_{max} is the frequency of the peak of the spectrum. β was calculated by using the measured $S(\omega)$ and plotting the value of β vs. ω. In all of the spectra, β appeared to come to a constant value where $\omega > .2$ Hz.

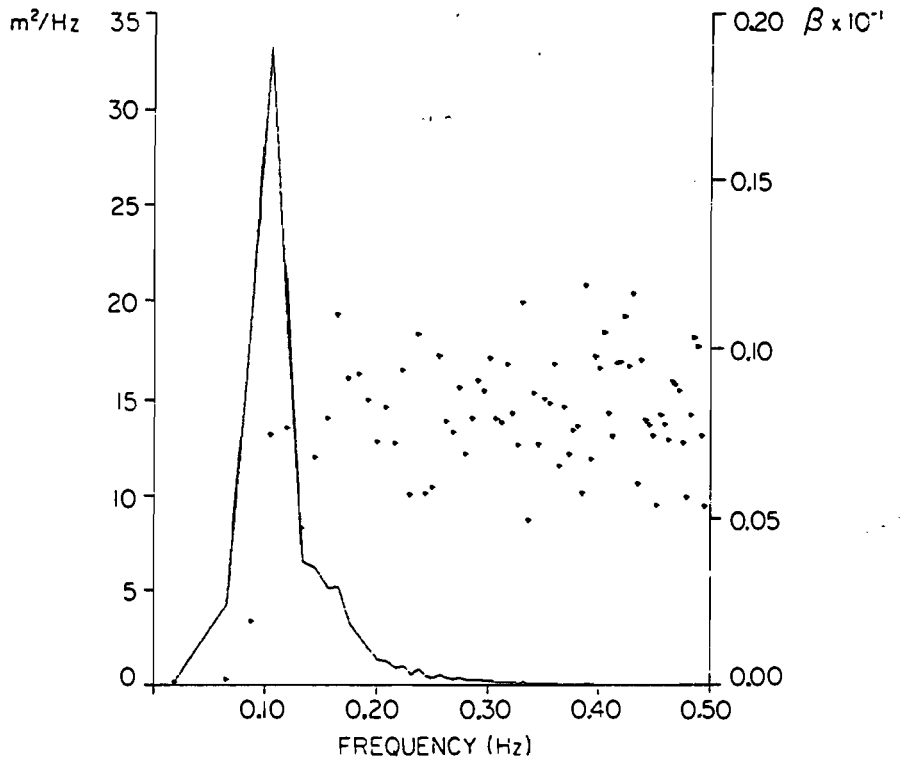

Figure 3.8 Doppler-corrected wave spectrum solid line shows the energy the asterisks are plotted values of β. β was calculated from Phillips relation $S(w) = \beta g^2 w^{-5}$ using measured values of S(w) for each frequency increment.

In previous experiments (Liu and Ross, 1980), Ross (1973), laser spectra measurements have agreed very well with wave rider spectra.

3.2 Flux Measurements

The flux measurements were made from the NOAA WP-3D research aircraft equipped with a boom-mounted multivane gust probe system (Bean and Emmanuel, 1980). Aircraft make excellent platforms for overwater research in that they are unaffected by sea motion and are relatively unaffected by salt and particle contamination (sensors may be cleansed with distilled water before and after each flight, as well as during the flight, by flying through rain or clouds, and may still operate under high wind conditions).

One disadvantage is that the instrumentation required for resolving atmospheric scales of 100 m or less must have a time constant considerably less than 2 ms; thus, instrumentation is required with faster response than that commonly used on towers and buoys.

Highly detailed mapping of meteorological variables in both time and space can be achieved when atmospheric and oceanographic measurement systems are coupled to the aircraft's inertial navigational system (INS).

3.2.1 Inertial Navigation System

The process of determining the three-dimensional wind vector referenced to the local earth coordinate system via the INS involves the vector sum of angles (pitch, yaw, roll). To maintain the inertial reference-frame coincident with the local earth coordinate system, the proper aircraft altitude, earth curvature, and rotation are combined to form a feedback control loop accomplished by a dedicated computer. The

aircraft's horizontal and vertical velocity components and position are derived from integration and double integration of the horizontal, and vertical accelerometer outputs. The altitude calculation requires the internal vertical accelerometer output, and an external altitude reference such as a barometric altimeter or, for low levels, an FM-CW radar altimeter.

Typical INS manufacturers' published error values are:

(1) average horizontal velocity error of ~1 m s^{-1},

(2) average vertical velocity error of ~10 cm s^{-1},

(3) aircraft altitude angle error of ~1 arc min, and

(4) radial position error to be within 2.5 km at the end of the first hour of flight.

There are, however, ways of improving on these specifications by utilizing 'Omega' navigation to update position. The Kalman filter (NATO, 1970) yields an unbiased, minimum-variance, linear estimation of the navigation parameters. By returning the aircraft to the same spot on the airfield immediately upon landing, one may determine the practical, or field residual, errors of the navigation system. The averaged results of such a test are listed in Table 2, where the manufacturer's specifications are seen to be met by the residual errors after long research flights involving intricate patterns and many turns (Bean and Emmanuel, 1980).

TABLE 3.1

Typical Omega-Inertial Performance

Total flights:	27
Total flight time:	281 hr
Average flight duration	8.1 hr
Average position error:	2.6 km
Average velocity error:	0.26 ms^{-1}
Position error rate	0.10 m s^{-1}

3.2.2 Turbulence Instrumentation

The sensor package for the turbulence measurements is normally mounted on a boom that extends 3 to 5 meters and is attached to the nose of the aircraft.

The sensor package includes:

(1) a gust probe for air velocity measurements,

(2) a small bead thermistor for temperature measurement,

(3) a microwave refractometer cavity for water vapor measurements.

The sensors are located at a distance of about one meter or less from each other to minimize the time of transport of air between sensors to about one-tenth that corresponding to the highest practical frequency that can be recorded.

The gust probe, which measures fluctuations in the components of the wind, consists of two vanes placed on the boom--the horizontal vane measures the vertical force of the wind and, hence, the vertical wind, w; a vertical vane measures the horizontal crosswind, v. A centrally located pitot tube measures the fluctuations in the along-axis wind. All three of these components are corrected for motion of the aircraft--primarily pitch, roll, and yaw, as well as for motion due to the boom as measured by accelerometers located on the gust probe and at the INS. A schematic of an overall system is shown on Figure 3.9, while typical measurement errors are given in Table 3.3.

Details of the procedure for wind tunnel calibration required by the gust probe system is given by Bean and Emmanuel (1980).

Temperature is measured with a small bead thermistor chosen for reliable stability, low noise, and uniform characteristics. Since the thermistor is mounted on a relatively fast-moving aircraft, a correction is made for dynamic heating. This is done both in the wind tunnel and in flight in clear, quiet air via the expression

$$T_a = T_i \ (1 - 0.20 \ \chi \ M^2)$$

where T_a is the ambient temperature (°C), T_i is the indicated temperature (°C), M is the Mach number, and χ is the form factor. The form factor for a bead thermistor varies from about 0.5 to 1.0. Typically, research aircraft travel at about 100 m s^{-1} (M = 0.294) with a resultant dynamic heating of 5° to 6°C. T_a can be determined from a vortex thermometer which decelerates the ambient air; its sensing element is a

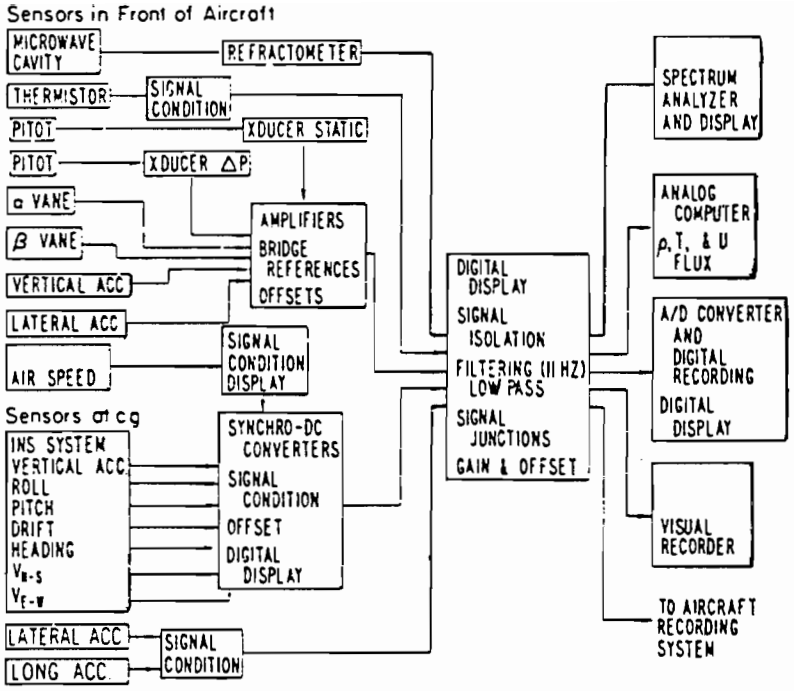

Figure 3.9 Schematic diagram of aircraft gust probe system.

TABLE 3.2

Published instrument Errors (rms) due to response of sensors of an Airborne Gust Probe System

Parameter	Typical Values	Error	Units
u'	1.0	2×10^{-2}	$m\ s^{-1}$
w'	0.3	6×10^{-2}	$m\ s^{-1}$
T'	0.4	0.5×10^{-2}	°C
ρ_v'	0.6	1×10^{-2}	$g\ m^{-3}$
$u'w'$	0.4	1.2×10^{-2}	$m^2\ s^{-2}$
$T'w'$	0.4	1.2×10^{-2}	$°C\ m\ s^{-1}$
$\rho_w'w'$	0.2	1.2×10^{-1}	$g\ m^{-2}\ s^{-1}$

NOTE: Errors are exclusive of aircraft platform effects and, therefore, do not constitute the entire error in the measurement.

bead thermistor. The form factor can then be determined from the above equation.

Conventional methods of measuring humidity do not have adequate response for flux measurements. The microwave refractometer has been suggested as an instrument that could overcome these difficulties (Hay, 1980). Use of a microwave refractometer in conjunction with other sensors permits the refractivity, temperature, and pressure of the atmosphere to be measured accurately to at least 10 Hz, permitting determination of fluctuations in water vapour density to 10 Hz. The absolute accuracy of the microwave hygrometer is 0.2 grams - m^{-3} and the resolution is 0.02 grams - m^{-3}.

3.2.3 Processing Methods

The high-frequency vibrations of the probe mounts and the natural resonance of each individual sensor require all signals to be low-passed with identical filters prior to being digitized. To reduce aliasing errors (*i.e.*, to less than 1%) active filters are used in conjunction with a sampling rate well in excess of the desired upper frequency of interest. All signals must be filtered identically due to the phase lag introduced by all analog filters. The results of tests normally encourage one to introduce, prior to the recording of the signals from the sensors, a rather sharp low-pass filter with a decrease of about 24 dB per octave. (The ERL boundary layer dynamics group employs a four-pole, Butterworth filter with a cutoff frequency 3 dB down at 11.5 Hz, well below the resonant frequency of the boom; a sampling rate of 80 Hz is used; the desired upper frequency limit is 10 Hz.) Additional filtering is done digitally during the numerical data reduction.

Processing of the data obtained by the gust probe system is subject to all of the usual pitfalls of experimental investigations, plus the added complexity arising from the intermittent nature of atmospheric processes. Intermittent means that a significant portion of the desired signal is contained in a small portion of the record; that is, the signal tends to come in random bursts. It is difficult to devise an automatic data-editing procedure to remove blanks of spurious spikes in the data that will not also edit the bursts. Consequently, such data require a great deal of visual examination to distinguish signal from noise. Care must also be taken when examining spectral properties. It is prudent to low-pass filter the data by averaging successive measurements such that the Nyquist frequency reflects the highest frequency of interest. In addition, any linear trend should be removed (the linear correlation coefficients between the variables and time are normally quite small; thus, there is usually very little trend). The data are then recalculated relative to the regression line. If the resultant spectra display significant spurious high energy at low or high frequency, one returns to a visual examination of the data to determine if higher order filtering is required.

An example of the above procedure is illustrated on the 'flow chart' shown on Figure 3.10. Note that the basic flight level parameters are recorded at 1 Hz, while the turbulence parameters are recorded at either 80 or 40 Hz. The basic operating tape is the WRT (Wind, Rho-v, and Temperature) tape. Note that detrending occurs at almost every step in the processing for the turbulence data.

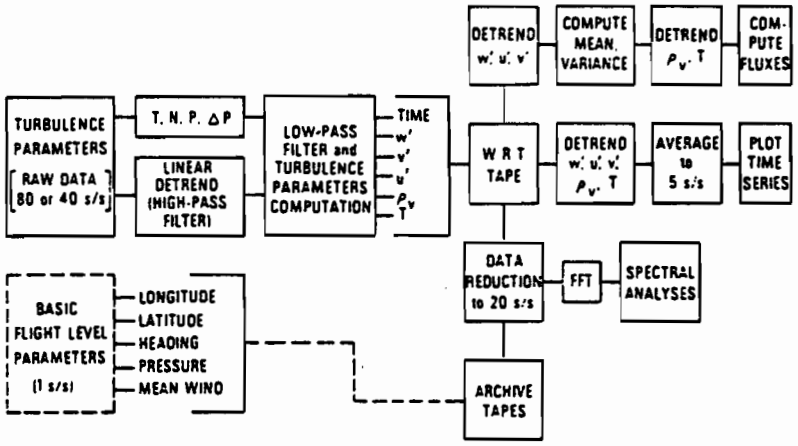

Figure 3.10 Aircraft data processing flow chart.

3.3 Bulk Measurements

Flight level measurements were made of wind speed and direction and temperature and humidity.

Wind and temperature measurements were corrected to a standard height of 10 m before they were compared or used in calculating drag coefficients following methods described in Reynolds (1982). The diabatic surface-layer profile proposed by Businger *et al.*, 1971, was used as a model. The input parameters for any sample were:

Wind speed u

Potential Temperature θ

Heights of u z_u

Heights of θ z_θ

Sea Surface Temperature θ_s

An iteration procedure was used to correct u and θ to a standard height $z = 10m$ in which:

Friction Velocity u_*

Scale Temperature θ_*

Obukhov Length L

Roughness Length z_o

were intermediate parameters. The iteration procedure was initialized by setting $z_o = 5 \times 10^{-5}$ m and the dimensionless height $\zeta = z/L$ to be equal to the bulk Richardson number

$$\zeta = R_{ib} = \frac{g(\theta-\theta_s)(\bar{Z} + Z_o)}{Tu^2}$$

where T is the average absolute temperature in °K, $\bar{z} = \frac{1}{2}(z_u + z_\theta)$. Humidity effects on buoyancy were not considered in the correction. Following Businger, 1973, we computed:

$$u_* = \frac{ku}{\ln \frac{z_u}{z_o} + \psi_1(\zeta)}$$

and

$$\theta_* = \frac{k(\theta - \theta_s)}{0.74 \ln \frac{(z_\theta)}{z_o} + \psi_2(\zeta)}$$

where k is von Karman's constant 0.4. For the stable cases

$$\theta_s < \theta \qquad \psi_1(\zeta) = \psi_2(\zeta) = 6\zeta \qquad \zeta > 0$$

In the unstable case $\theta_s > \theta \qquad \zeta < 0$

$$\psi_1(\zeta) = -2 \ln[(1 + x)/2] - \ln[(1 + x^2)/2] + 2 \tan^{-1}(x) - \frac{\pi}{2}$$

where $x = (1 - 16\zeta)^{\frac{1}{4}}$

$$\zeta_2(\zeta) = -2 \ln[(1 + y)/2]$$

$$y = (1 - 16\zeta)^{\frac{1}{2}}$$

The iteration was closed by calculating z_o from u_* by Pierson's (1978) formula. The function chosen for z_o was somewhat arbitrary, and Pierson's function was used because it was deduced specifically from marine environments.

$$z_0 = \frac{3.905 \times 10^{-5}}{u_*} + 0.001604\, u_*^2 - 1.74565 \times 10^{-4}$$

The new value was compared to the previous one, and the iteration was repeated with

$$\zeta' = g\theta_* \, k(\bar{z} + z_o')$$

The solution was complete when z_o' was within 5% of z_o. The loop converged usually with less than five iterations on a PDP-11/55. Finally U_{10} and θ_{10} were computed by:

$$U_{10} = \frac{u_*}{k} \ln\left(\frac{z}{z_o}\right) + \psi_1(\zeta')$$

and

$$\theta_{10} = .74 \frac{\theta_*}{k} \ln\left(\frac{z}{z_o}\right) + \psi_2(\zeta') + \theta_s$$

AXBT surface temperature values were used for determining θ_s. Downward-looking PRT-5 radiometer data was available and was used when it was calibrated by the AXBT temperatures.

4. CHAPTER IV: RESULTS

4.1 15 November 1980

In examining the effect on the drag coefficient and the surface fluxes of changing wind direction and wind speed which accompany a frontal passage, we find that the rapid change in wind direction caused by a frontal passage will put the ocean surface wavefield into local disequilibrium with the new windfield.

4.1.1 Frontal Motion 15 November

On 15 November 1980, a very strong frontal system was investigated using the NOAA P-3 to fly through the front in the boundary layer. Figure 4.1 shows the surface analysis for 15 November 1200Z. Figure 4.2 shows the surface analysis in the area near the front for 16 November 0000Z. The frontal motion is clearly evident. Two frontal penetrations were made, the first penetration was westbound at low level $\sim$ 300 meters, immediately after the front was passed, the aircraft descended to 150-m altitude for the rest of the flight. Figure 4.3 shows the flight track of the P-3 for the westbound leg of the mission. The location of the frontal penetration was determined by locating the time of change of wind direction. The front was located at 138.14°W longitude at 2200 GMT 15 November on the westbound leg. On the eastbound leg, penetration was made at 134.97°W longitude at 0143Z 16 November. Satellite photos of the area showed the frontal motion to be nearly west to east; therefore, the frontal motion was considered to be west to east only at 49°N, the latitude of the study area. The front was moving at 64.1 km/hr.

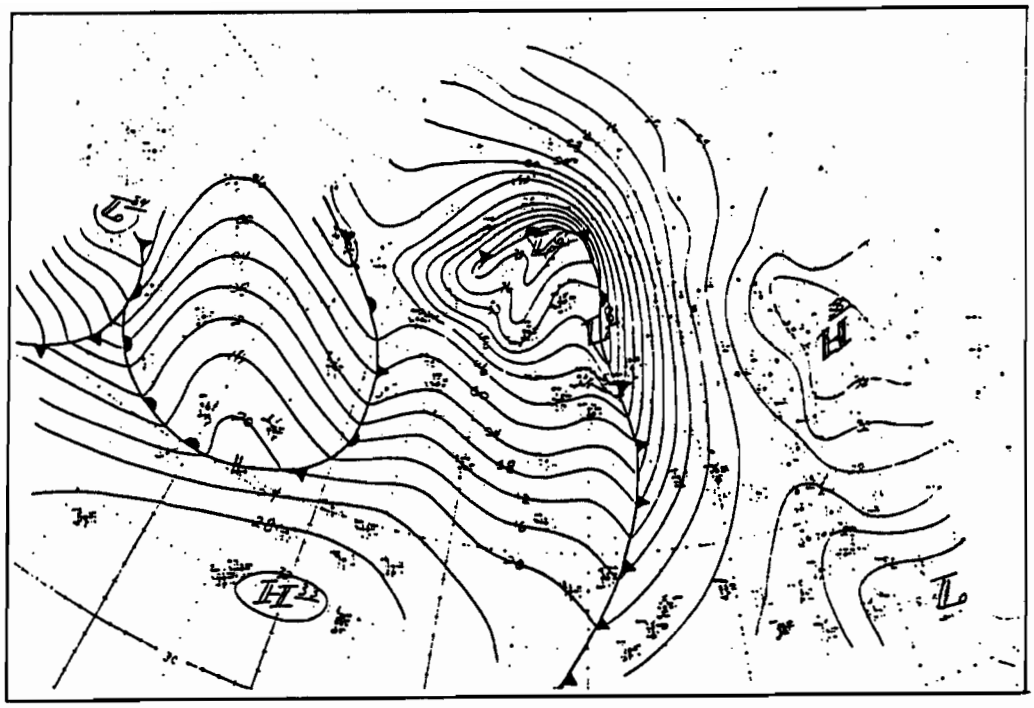

Figure 4.1 Surface analysis for 15 November 1200Z.

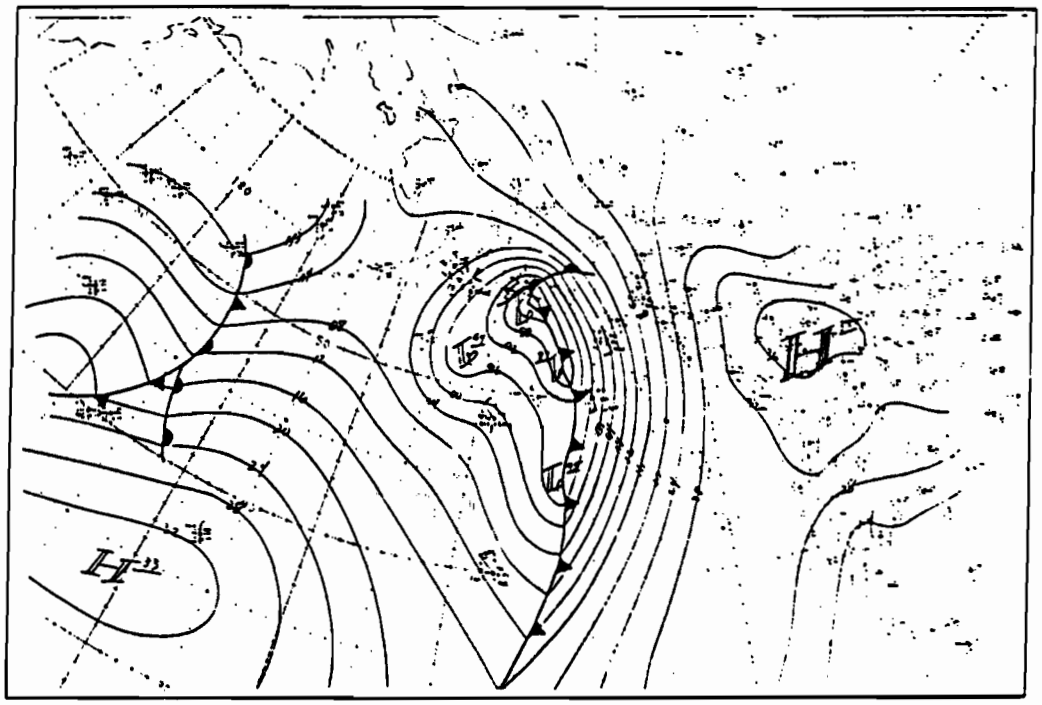

Figure 4.2 Surface analysis for 16 November 0000Z.

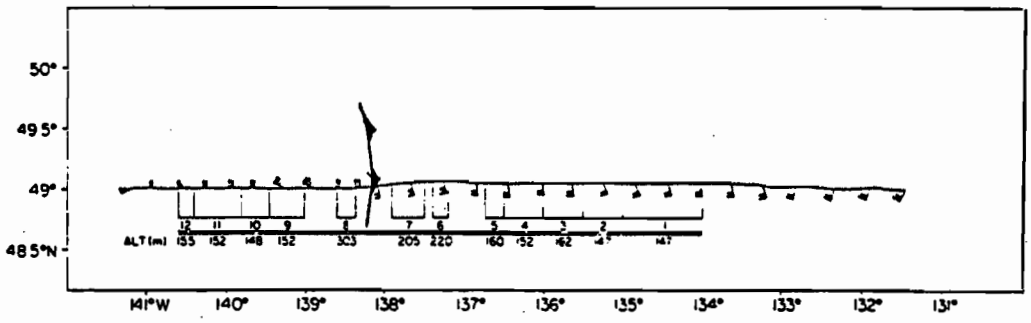

Figure 4.3 Aircraft track in the cold sector, wind barbs show the wind speed and direction at aircraft altitude. The sequence of numbers above the double line show the stress files for the westbound penetration 1-12. The numbers below the double line show the average aircraft altitude in meters for each of the files. The light vertical lines mark the boundaries of the files.

The distances from the front to the position of wave spectra estimation and to the position of the momentum flux measurements were calculated by taking the midpoint of the flight segment that made up the laser runs and eddy correlation runs. The laser flight segments were limited to ∿ 18 km of flight segment. The eddy correlation flux runs varied in length from ∿ 12 km to ∿ 45 km.

In addition, a surface wind speed analysis was derived from vertical camera photography using an assessment of surface-foam and whitecap coverage. Figure 4.4 shows the surface wind-speed estimate from the two methods plotted as a function of increasing distance into the cold sector from the front. It is noteworthy that the foam coverage surface winds drop below the phase speed of 6-sec waves at the distance where both the drag coefficients and the 6-sec wave energy drop.

Comparisons were made between U^{10} measured at the GOES meteorological buoy (Reynolds, 1982) located at 50°N and the aircraft measurements reduced to 10-m heights by the method outlined in Chapter 3. Since the aircraft did not fly directly over the GOES buoy, representative values of the wind speed were taken from ahead of and behind the front. Figure 4.5 presents the data taken during the frontal passage by the GOES buoy. The front is clearly evident as a rapid turning of the wind from 180° to 270° together with a change in air/sea temperature from 2° stable to 4° unstable immediately behind the front tending to 2° unstable several hours after the frontal passage.

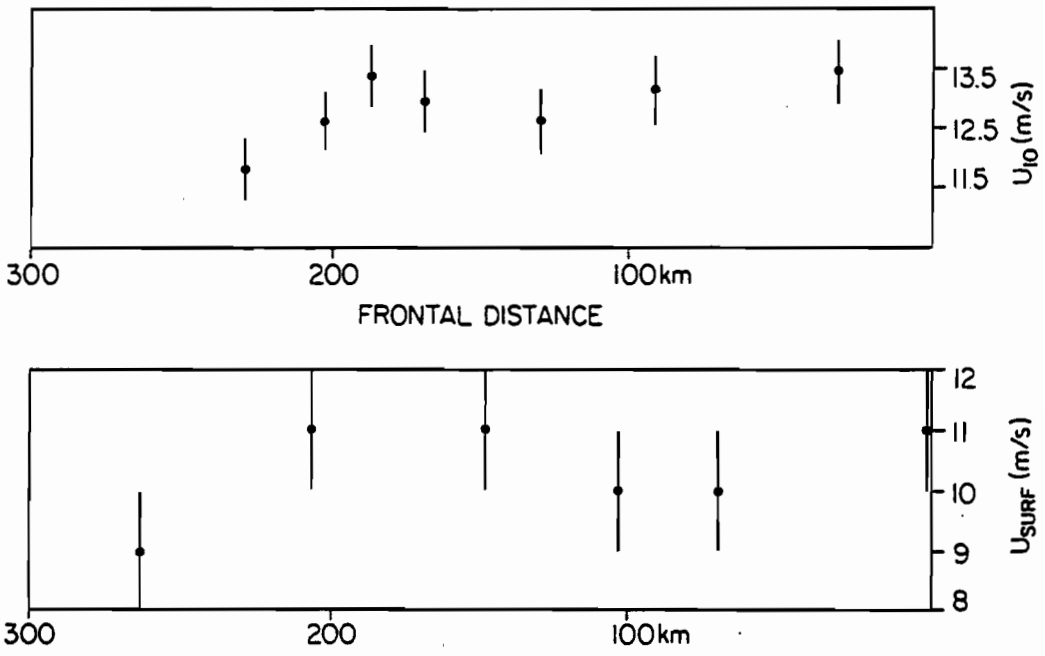

Figure 4.4 Surface wind speed vs. frontal distance for the 15 November 1980 westbound frontal penetration. *Upper panel*: The wind speed at 10 meters calculated from the aircraft level wind speed measurements and corrected for stability. *Lower panel*: The estimated surface wind speed from vertical camera photography using foam coverage estimates.

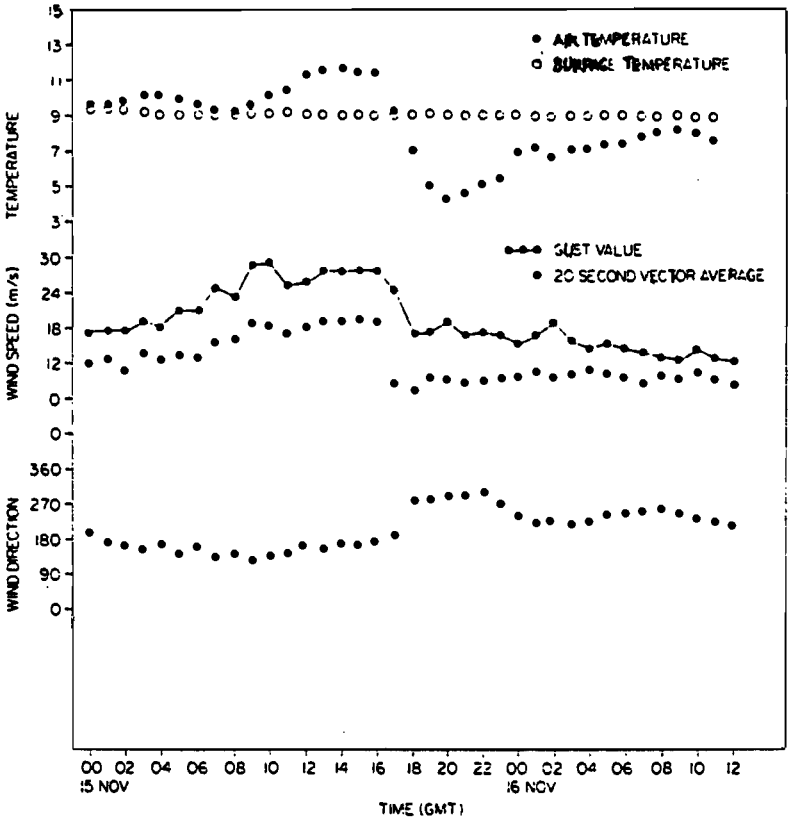

Figure 4.5 GOES meteorological data buoy time series during frontal passage. The buoy was located at station P′ ~ 140°W 50°N.

4.1.2 15 November Flux Measurements

Flux measurements were made continuously during the low-level flight segments. The westbound frontal penetration began in the warm sector ahead of the front, which was characterized by a stable atmosphere and high winds >20 m/sec^{-2}. Most of the flux measurements were made in the cold sector where the wind speeds were between 11.5 and 14 m sec^{-1}. Table 4.1 is a tabulation of the flux measurements and other parameters. The momentum flux, τ, measured at 150-m altitude was corrected to a standard height, 10 m, using a value for $\frac{\partial \tau}{\partial z}$ computed by measuring the turning angle of the wind from the geostrophic level to height of the surface layer. However, there were no reliable measurements of surface wind speed and direction in the area of the aircraft flight track. Therefore, the surface wind speed and direction were taken from model values calculated by Brown (1982). In the cold sector, the air/sea temperature difference was always between 2°C and 3°C unstable. Brown's model predicts that the surface winds would be turned ~10° to the geostrophic and reduced in velocity to .85 Vg, where Vg is the geostrophic value.

It was found by comparing the aircraft winds with the surface layer winds calculated by Brown's model that the aircraft level (150-m) winds were identical to the surface layer winds from the model. The height corrections to $u'w'$ were applied to all of the stress files for both sides of the front. The frontal distance was calculated for the stress files in the cold sector since the side of the front was where we expected to see the variations due to a changing sea state. On the warm side, the sea state was determined in one location since the warm sector had had time for the wind and the wave field to reach dynamic

FLUX MEASUREMENTS OF 15 NOVEMBER 1980

File #	Time GMT	Altitude Meters	U_{alt}	τ/ρ m^2/sec^2	$C_{dn}x10^{-3}$	U_{10}	L	Tv	T_{10}	T_s	Frontal Distance
					WARM SECTION						
1	2119	148	28.9	1.35	3.22	20.7	890	13.0	13.7	12.3	
2	2129	150	28.8	1.58	3.85	20.4	794	1.31	13.8	12.2	
3	2134	154	28.8	1.35	3.36	20.2	707	13.1	13.7	12.0	
4	2139	152	28.8	1.13	2.88	20.0	597	13.0	13.5	11.5	
					COLD SECTION						
8	2203	301	16.6	.326	1.75	13.4	-291	14.7	7.9	9.6	30 km
9	2211	153	15.5	.200	1.06	13.2	-139	15.7	7.1	10.4	92
10	2217	149	14.7	.144	0.86	12.5	-128	15.2	7.0	10.2	128
11	2221	153	15.3	.266	1.44	12.9	-149	15.3	7.2	10.2	169
12	2229	156	14.9	.515	3.05	12.5	-191	16.3	8.1	10.3	203
13	2254	152	13.8	.377	2.50	11.7	-159	16.2	7.9	10.2	229
14	2301	152	15.9	.584	3.03	13.4	-171	15.6	7.4	10.3	188
15	2309	150	14.7	.311	1.91	12.4	-166	16.0	7.8	10.3	175
16	2314	168	19.6	.272	1.73	12.3	-191	16.3	8.2	10.3	172
17	2319	168	14.2	.275	1.83	11.9	-176	16.5	8.3	10.3	168
18	2322	168	14.3	.238	1.50	12.1	-140	15.4	7.3	10.1	166
19	2333	56	13.7	.253	1.60	12.2	-173	17.3	8.0	10.3	164

U_{alt} - mean wind speed at aircraft altitude
C_{dn} - neutral drag coefficient at 10-meters altitude
L - Obukov length
T_v - virtual temperature at aircraft altitude, U_{alt}
T_{10} - virtual temperature at 10-meters altitude
T_s - surface temperature from the PRT-5 radiometer

TABLE 4.1

equilibrium. The bulk aerodynamic formulas which parameterize the air/sea fluxes in terms of the mean wind speed (U(z)), potential temperature $\theta(z)$ and abolute humidity q(z) at a height z, the surface humidity q_s and sea temperature T_s are:

$$- uw = C_d U^2(z)$$
$$wt = C_T U(z) \Delta\theta$$
$$wq = - C_E U(z) \Delta q$$

where $\Delta\theta = T_s - \theta(z)$ and $\Delta q = q_s - q(z)$. The air/sea temperature difference ΔT and air temperature T_z are

$$T_Z = \theta(Z) - \theta Z$$
$$\Delta T = \Delta\theta + \gamma Z$$

where γ is the adiabatic lapse rate $0.01°K\ m^{-1}$.

4.1.3 Computed Drag Coefficients

The nondimensional drag coefficients can be determined by direct flux measurements and measurements of mean quantities. In order that the variation with height can be eliminated, the drag coefficient, C_d, is commonly evaluated at 10 m as C_{10}, using the wind speed at 10 meters U_{10}, obtained as in Chapter 3. We shall follow this method throughout this study. The stability dependence must be removed in order that comparisons may be made between measurements ahead and behind fronts. The dependence is removed by calculating the coefficient in the equivalent neutral case at 10 m, C_{dn}. Following Fleagle and Businger (1980),

$$C_d = C_{dn} \left[1 - C_{dn}^{\frac{1}{2}} \frac{\psi_1}{k}\right]^{-2}$$

$$C_d^{\frac{1}{2}} - C_d^{\frac{1}{2}} C_{dn}^{\frac{1}{2}} \frac{\psi_1}{k} = C_{dn}^{\frac{1}{2}}$$

$$C_d^{\frac{1}{2}} = C_{dn}^{\frac{1}{2}} + C_{dn}^{\frac{1}{2}} C_d \frac{\psi_1^{\frac{1}{2}}}{k}$$

$$C_d^{\frac{1}{2}} = C_{dn}^{\frac{1}{2}} \left[1 + C_d^{\frac{1}{2}} \frac{\psi_1}{k}\right]$$

$$C_d = C_{dn} \left[1 + C_d^{\frac{1}{2}} \frac{\psi_1}{k}\right]^2$$

$$C_{dn} = C_d \left[1 + C_d^{\frac{1}{2}} \frac{\psi_1}{k}\right]^{-2}$$

where k is von Karman's constant and ψ_1 is the diabatic correction as shown in Chapter 3 and evaluated at z = 10 meters.

C_d was calculated using the eddy correlation momentum flux measured at the aircraft flight level and U_{10} calculated from the corrected U_{150}.

Figure 4.6 is a plot of the drag coefficient C_{dn} and τ/ρ as a function of distance from the front. The surprising aspects of this figure are the dip in stress and C_{dn} immediately behind the front and the subsequent increase in stress and C_{dn} with greater distance from

the front. C_{dn} and the stress returned to the lower values when the frontal distance had exceeded 200 km.

The data set for the 15 November frontal passage allows us to use the measured eddy correlation momentum flux, and the bulk wind speed, U_{10}, to recover a drag coefficient that is independent of modeling errors. The wave spectral data will show the variations in energy density in the various parts of the surface wave spectrum. We will then be able to relate unambiguously the changes in the drag coefficient to the changes in the wave field.

4.1.4 Wave Field Spectral Analysis

A total of 20 wave spectra were computed (cf. Ch 3) for the two days of which 14 were calculated for the 15 November flight. After penetrating the front on the westbound leg, the aircraft flew nearly upwind for a distance of $\sim$ 250 km (see Fig. 4.3). The upwind direction allowed a nearly continuous measurement of the wave height with the laser profilometer. Wave spectra were calculated every three minutes using segments of flight track $\sim$ 18 km long which is long enough to provide adequate confidence limits to spectral calculations, but short enough to ensure homogeneity over the sample. Since laser wave spectral data are confined only to measure upwind or downwind, continuous wave data on the warm side of the front was unavailable due to the crosswind track of the aircraft through the warm sector. The wave spectrum in the warm sector was sampled at the end of the flight after the eastbound passage. This sample gave a good estimate of the wave spectrum in the stable warm sector.

On the 15th of November, the ship reports from both the *Oceanographer* at P´ and the *Vancouver* at Ocean Station P showed strong swell

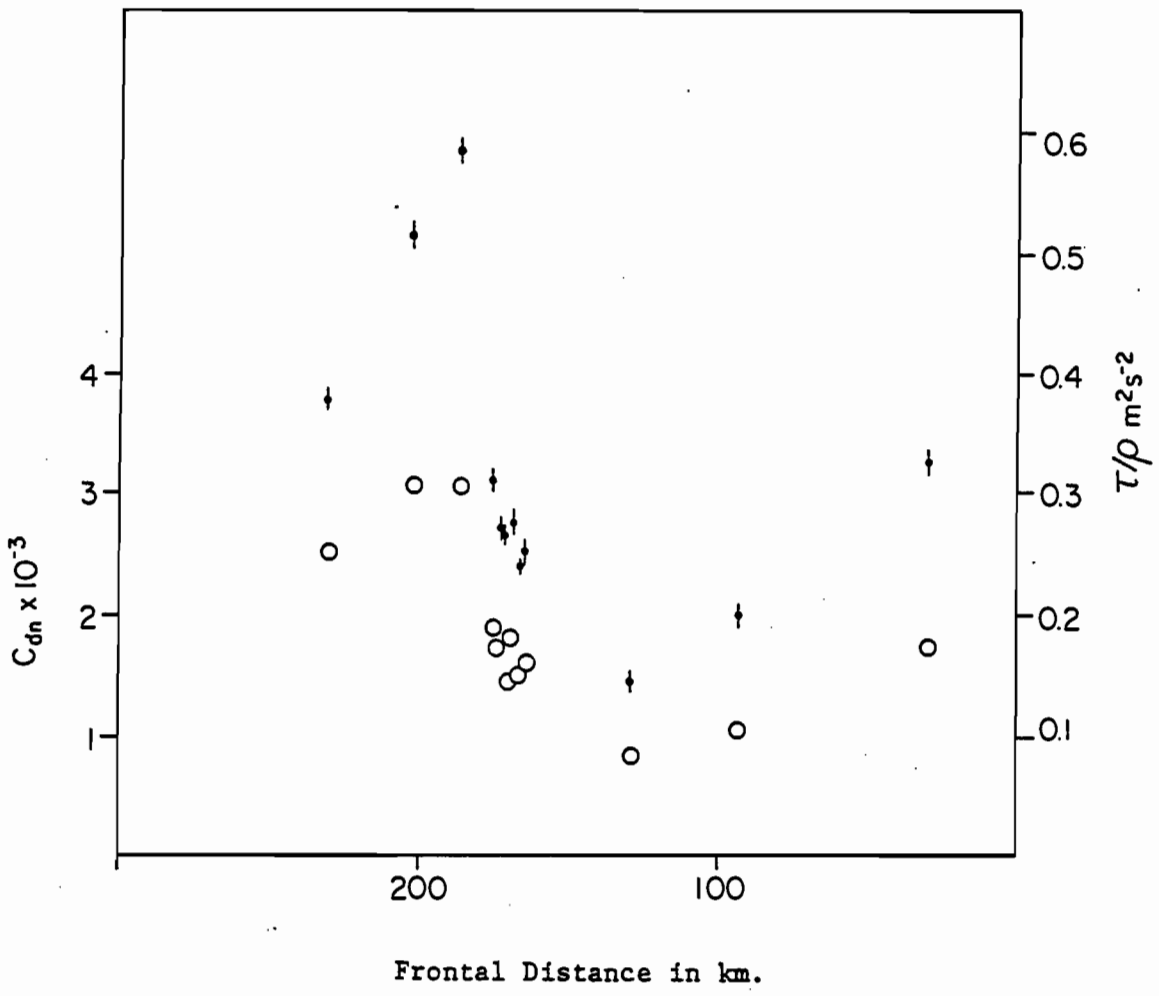

Figure 4.6 The drag coefficient C_{dn} shown by the open circles and the stress τ/ρ shown by for the upwind frontal penetration on 15 November 1980.

from the south ahead of the front. Immediately after the passage of the front at P, the *Vancouver* reported a dual swell system with the new swell pattern coming from the west (270°). The *Oceanographer* reported only swell from the south until some four hours after the frontal passage when it reported swell from the west. It seems unusual that the swell from the south would die so suddenly, and it is more likely that the observer reported only the dominant swell.

Using the position of the low-pressure center on the 15 November as a reference point, Ross's model for wave height predicted the surface wave spectral peak frequency significant wave heights to be respectively for the cold sector.08 sec^{-1} and 3.2 meters and .07 sec^{-1} and 7.6 m for the warm sector. Ross's model does not predict the distribution of wave energy in the spectra; however, his model did predict the same peak frequency as measured by the laser, but it slightly underestimated the significant wave height in the cold sector and overestimated it in the warm sector.

The peak frequency of the wave spectrum for the entire run upwind into the cold sector was .08 ± .01 cycles/sec. The peak frequency was stable to within the resolution of the spectral measurements. $H_{1/3}$ was nearly stable for the entire upwind run with an average of 4.13 meters and a standard deviation of 0.24 meters. Clearly the change in C_{dn} and τ could not be directly related to either of these two parameters.

Table 4.2 shows the values of the wave spectrum parameters for the upwind flight through the cold sector and the upwind spectrum calculation for the warm sector. The surface wave spectrum measured ahead of the front in the warm sector of the storm is shown in Figure 4.7. This spectrum has the typical shape as described in the JONSWAP report

LASER WAVE SPECTRA FOR 15 NOVEMBER 1980

Laser File Start Time	β x10^{-3}	6 sec energy m^2-sec	H 1/3	Peak Frequency hz	Longitude	Time	Frontal Position at Time	Frontal Distance km	Surface Wind Speed from Vertical Camera Observations m-sec^{-1}
						2200	138.14		12
2203	5.24	1.52	4.20	.079	138.46	2204:30	138.07	28.16	7
2206	8.46	1.63	4.19	.096	138.71	2207:30	138.03	49.10	
2209	10.70	2.62	4.59	.097	138.94	2210:30	137.98	69.33	10
2212	9.56	2.48	4.31	.08	139.14	2213:00	137.94	86.66	
2214	9.08	2.80	4.30	.08	139.35	2215:30	137.91	103.99	10
2221	8.08	2.90	3.92	.095	139.87	2222:00	137.81	148.77	11
2223	7.72	3.15	3.86	.094	140.07	2224:30	137.77	166.10	
2226	7.17	3.71	4.13	.095	140.31	2227:30	137.73	186.32	
2229	7.23	3.69	4.12	.079	140.55	2230:30	137.69	206.54	11
2232	7.79	3.72	4.19	.094	190.79	2233:30	137.64	227.49	
2235	6.54	3.17	3.63	.078	141.04	2236:30	137.60	248.43	
2237	6.74	2.91	3.92	.080	141.20	2238:30	137.57	262.15	
2241		1.69	3.92	.074	141.16	2242:30	137.51	263.60	9
					WARM SECTOR				
0203	7.76	4.47	5.28	.10	134.14	0204:30			

TABLE 4.2

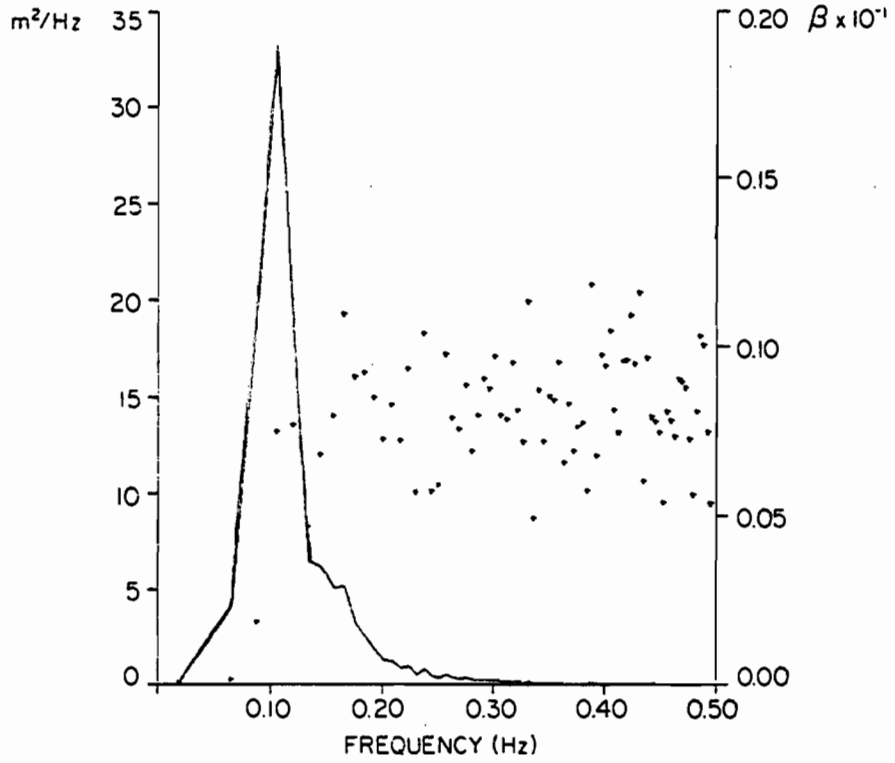

Figure 4.7 Warm sector wave spectra. The solid line shows the energy. The asterisks are the values of β calculated for each frequency increment. Note that the β values stablize very close to the peak of the spectrum.

(Hasselmann *et al.*,1973), a very steep front face and rapid drop behind the spectral peak which occurs at .10 Hz. Note especially that the values for Phillips' parameter reach equilibrium at the peak frequency, which implies that this spectrum does behave as Phillips' model predicts; that is

$$S(\omega) = \beta g^2 \omega^{-5}$$

Where $S(\omega)$ is the spectral density, β is a constant, and g is the local gravity. This spectrum is very likely in dynamic equilibrium with the warm sector wind field. One of the spectra from the cold side of the front, shown in Figure 4.8, exhibits quite a different spectral shape. The spectral peak here is less sharp and does not drop rapidly on the rear face. Moreover, notice that Phillips' parameter does not come to equilibrium until well beyond the region of maximum spectral energy, which implies that this wave field does not fit Phillips' model.

4.1.5 Definition of the Spectral Field

The final estimates of the spectral energy at various distances from the front are shown in terms of true frequency $f = \sigma/2\pi$, where f is frequency in cycles sec^{-1}, and the true frequency spectrum. Figure 4.8 shows contours of $F(f,x)$ m^2 s for the wave spectra. The spectral values were smoothed using hamming consecutive weighting factors. The 90% confidence limits were approximately 0.70 and 1.30. This presentation is similar to the type used by Barnett and Wilkerson (1967).

The contours on the f-x diagram are based on 14 values of $\bar{F}$ vs. f for each of 13 spectra. The x axis is shown representing the distance from the front into the cold sector, x equals zero at the position of

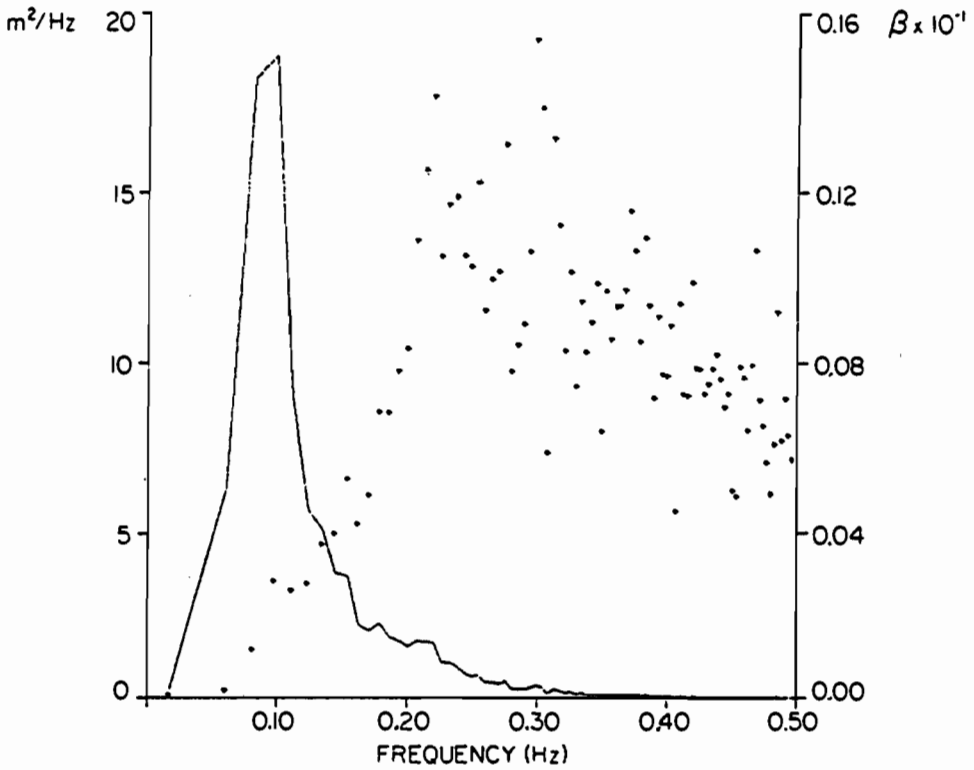

Figure 4.8 Cold sector wave spectrum. The solid line shows the energy. The asterisks are the values of β calculated for each frequency increment. Note that in this spectra the β values never stablize.

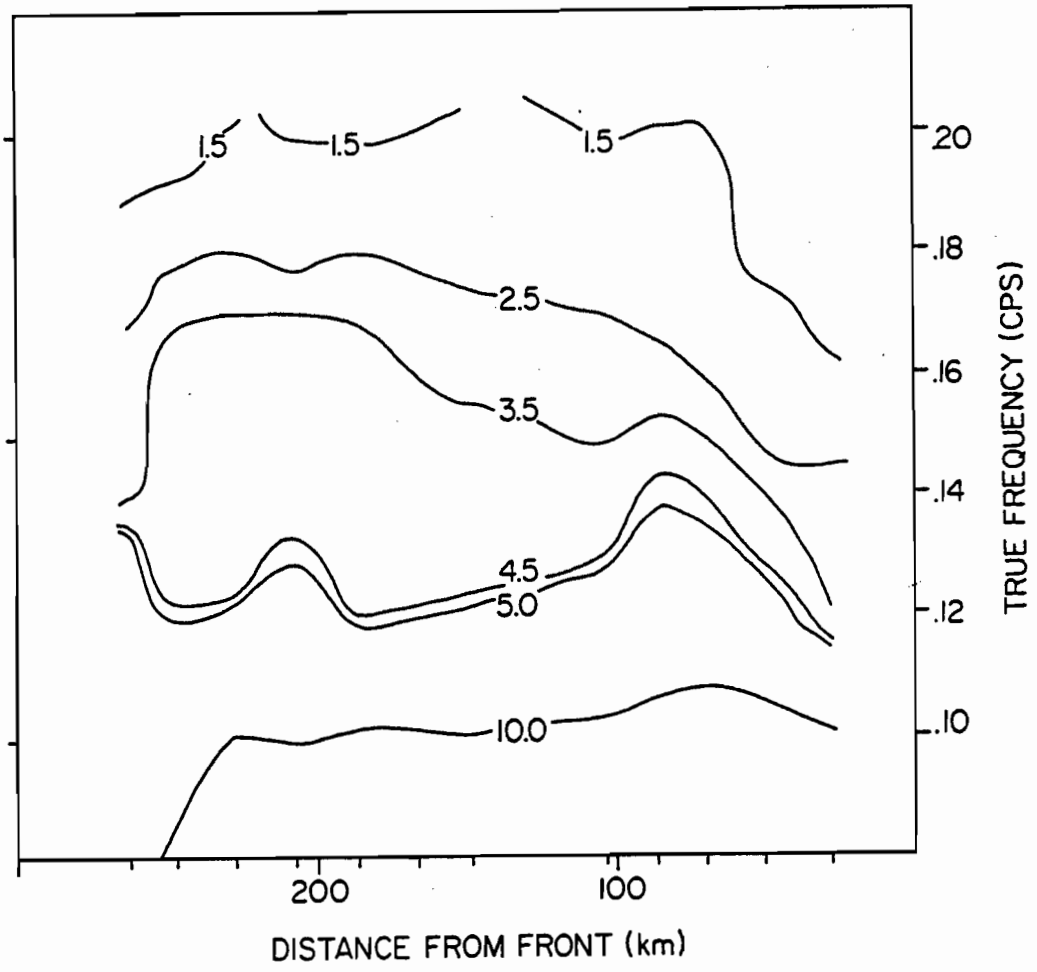

Figure 4.9 Contour plot of wave spectral energy in m^2-s at various distances from the front. The tick marks show location of the individual wave spectra.

the front. The position of the individual spectra are shown by the small ticks along the x axis.

In viewing the f-x diagrams, note that a cut along the f axis at constant x will give a spectrum F(f,o) at x and reflect the actual F(f,o) measured over the 18-km flight track.

Similarly, a cut along the x axis at constant f will give the spacial history of the f spectral component, showing the location of spectral peaks at any given x and enabling us to see that the lower frequencies always contain more of the energy when an individual frequency component is in equilibrium $\partial F/\partial x = 0$ and the contours will parallel the x axis.

The essential features of the diagram are:

(1) The major spectral peak occurs at frequencies below that expected for wind sea. We infer that a significant swell may be present.

(2) There is a tendency in the medium wavelength waves f = .126 hz for energy to increase to a maximum at 86 k from the front and then decrease until a secondary maximum occurs ∿206 km from the front.

(3) There is a considerable amount of wave energy in the low-frequency end of the spectrum for small values of x. We suggest that this may be due to remnant energy from the swell generated by the warm sector winds. However, Barnett and Wilkerson (1967) found similar energy at small values of x for fetch-limited conditions and speculated that the energy was being added simultaneously over the whole frequency range of the spectrum.

(4) There is an increase of wave energy in the higher frequencies with distance behind the front until a region is reached where the wind speed decreases and the waves go from being underdeveloped and moving slower than the wind to being swell. This increase of energy at higher frequencies is an unexpected phenomenon because it requires the slower moving waves to increase in energy and wave height, thereby creating roughness elements that are high and appear to be moving slower as the distance into the cold sector increases.

Look, for example, at the 3.5 m^2-sec contour at 100 km distance; it corresponds to the ∿.15 hz frequency. At this frequency, waves have a phase velocity c_p = 10.4 m/sec. At 227 km from the front the 3.5-m contour has moved up to .173 hz, at this frequency waves have a phase velocity C_p = 9.01 m/sec. If the drag due to these elements is a function of the square of the velocity deficit computed using U_{10}, there will be a factor of 2 increase due to the change in phase speed of the waves.

The more interesting aspect of the duration-limited case is the constant increase in energy of the shorter gravity waves until the aircraft moves into a region where the wind speed drops. This increase in wave energy departs markedly from previous (*i.e.*, fetch-limited) studies where the wave energy tends to peak for a particular frequency at some fetch distance and then as the fetch increases, the energy at that frequency decreases to a lower equilibrium value. The increase and then decrease of wave energy in spectral bands is known as *overshoot* (Barnett and Wilkerson, 1967). We will see that the region where the

higher frequency energy reaches a maximum corresponds to the maximum in air/sea momentum flux and drag coefficient.

Figure 4.10 shows the values of β and energy density in the six-sec wave field, E_6, for the wave spectra measured on the westward passage through the front. It can be seen that the energy in the saturated part of the spectrum, characterized by the value of β, at first increases rapidly immediately behind the front, and then decreases towards an equilibrium value as the measurements proceed farther into the cold sector. The energy density in the six-sec waves is rather low immediately behind the front but increases systematically to a maximum approximately 200 km behind the front. It then decreases at larger distances behind the front.

The region of the wave spectrum which is of most interest is the region in which the phase speed of the waves is less than the surface wind field. We can see from Figures 4.6 and 4.9 that the energy in the six-second wave fields, which are the largest waves moving slower than the wind, correlate well with the increase in C_d. Closer to the front, before the six-second wave field has a chance to develop, the drag is controlled by the even shorter, slower waves in the saturation region of the spectrum which is characterized by Phillips' parameter β.

In the early stages of new wave field development, the shorter waves quickly saturate, β rises to a high value then decreases to more or less an equilibrium. As the shortest waves are returning to equilibrium, the next longest waves are increasing due to direct interaction of the wind. During the initial stages of wave growth, the small-scale waves support the drag. As their energy and height decrease, the drag coefficient begins to decrease. The nonlinear energy

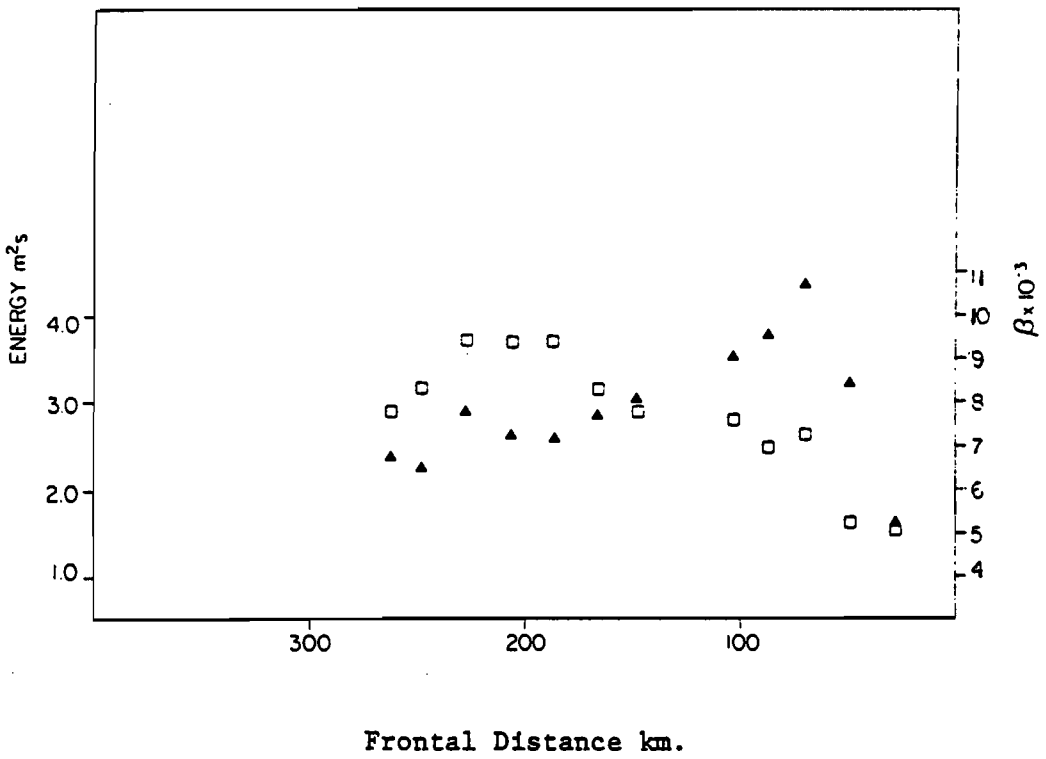

Figure 4.10 Energy density in the 6-second wave field .154hz→.174 hz,□. Phillips' constant β,Δ for the upwind frontal penetration 15 November 1980.

exchange mechanism (Hasselmann *et al.*, 1973) starts to build the six-second wave field and as the shorter waves decrease, the six-second waves grow and the increase is correlated with the increase in the atmospheric drag. Finally, at a distance of ∿ 240 km from the front, the surface wind speed drops below the phase velocity of the six-second waves (see Fig. 4.4). The waves are transformed directly from an underdeveloped sea state into swell. The momentum flux decreases, and the drag coefficient decreases towards a lower value.

Figure 4.11 shows β as a function of U_{10}. We can see that there is a tendency for β to increase with increasing U_{10}. However, there is more spread in the β values due to their position relative to the front at the same wind speed than to changes in U_{10}. Note in Figure 4.10 the rapid rise in β as the measurements proceed into the new wind regime. The rapid change in β may be related to the change in radar backscattering cross section observed in scatterometer data across the regions.

4.2 7 November Data

The data set of 7 November was used as a second case study for comparison with the 15 November frontal data set. Figure 4.12 shows the surface analysis for 8 November 0000 Z. The 7 November data were taken under similar stability conditions to the 15 November data (*e.g.*, ∿ 2°) unstable with slightly lower winds in a very homogeneous post-frontal regime. In particular, the wind speed and direction had been constant for ∿ 36 hours leading to a sea state which should have been completely in equilibrium with the local prevailing wind. The area was somewhat to the west of the 15 November flight but was definitely a post-frontal regime. The flight segment of interest was the upwind leg

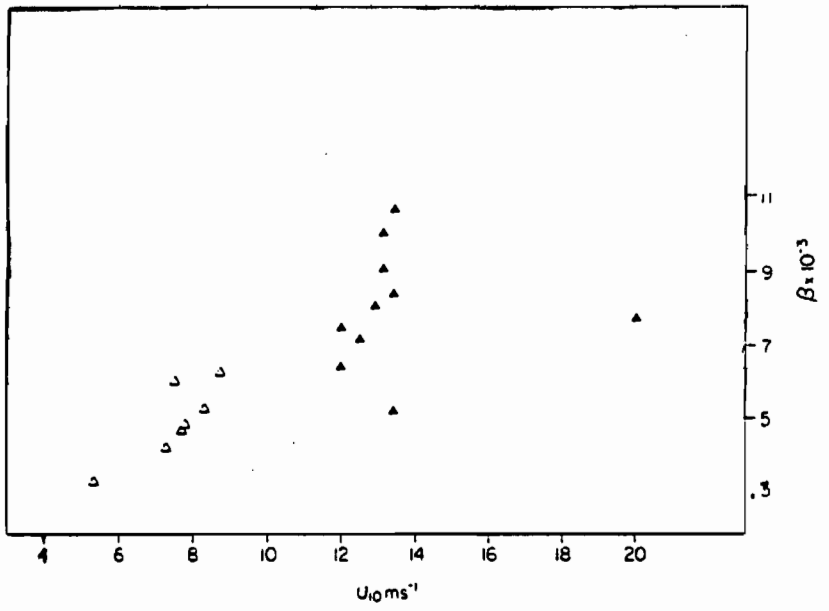

Figure 4.11 Phillips "constant" β as a function of U_{10} for Δ 15 November, Δ 7 November upwind flight segments.

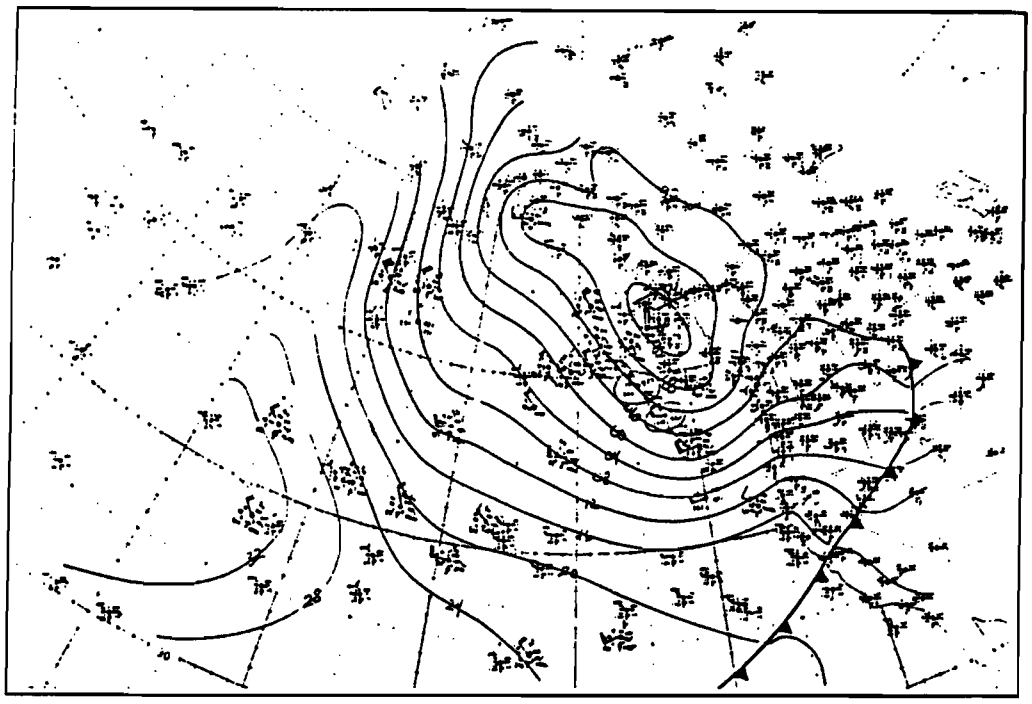

Figure 4.12 Surface analysis for 7 November 1200Z.

starting at 0351 Z 16 November at 48.67°N 141.21°W and running northwest to ocean station P. Figure 4.13 shows the flight track and the center points of the flux segments and laser segments. Figure 4.14 shows the surface wind analysis of 7 November given by Brown's Planetary Boundary Layer model (Brown, 1982). The aircraft measurements were all made at an altitude of 50 meters. The wind speed at flight level varied along the track from a high of 9.7 m/sec to a low of 5.8 m/sec. The surface wave spectra and Phillps' parameter, β, were calculated for the 7 November data in an identical manner as the 15 November data. Table 4.3 and 4.4 show the values of the momentum flux and wave spectral parammeters. Figure 4.14 shows a plot of τ/ρ, and C_{dn}, for the 7 November upwind segment on the same horizontal scale as the 15 November frontal passage. Figure 4.15 shows a plot of β and E_6 for the 7 November upwind segment.

For most of the upwind segment, the atmosphere was approximately 2°-2.5° unstable which was very similar to the 15 November cold sector stability.

With the exception of a single value which was measured during a rain squall, the equivalent neutral drag coefficients for the 7 November upwind segment show a good correlation to the β parameter. It should be noted that the increase in C_{dn} at 0121 GMT correlates with the increase in β. β was increasing because from 0118 to 0121, U_{10} increased from 5.4 m/sec to 8.2 m/sec. This freshening of the wind immediately begins rebuilding the short gravity wave field as can be seen by the increase in β.

The increasing wind places the wave field in disequilibrium with surface wind causing the increase in C_{dn}.

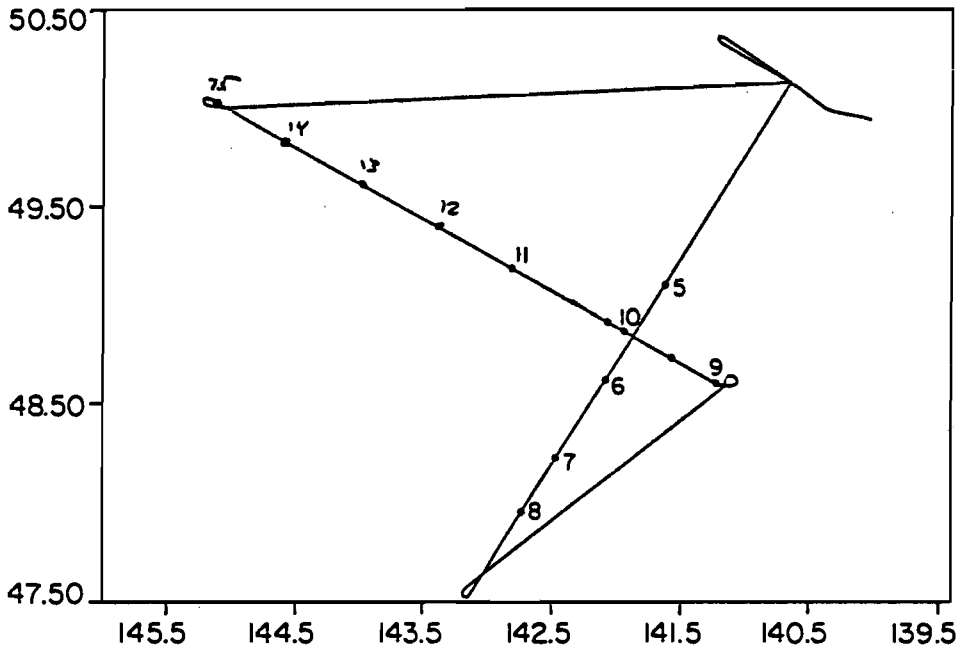

Figure 4.13 Flight track for 7 November 1980. Numbers indicate center of momentum flux file measurements.

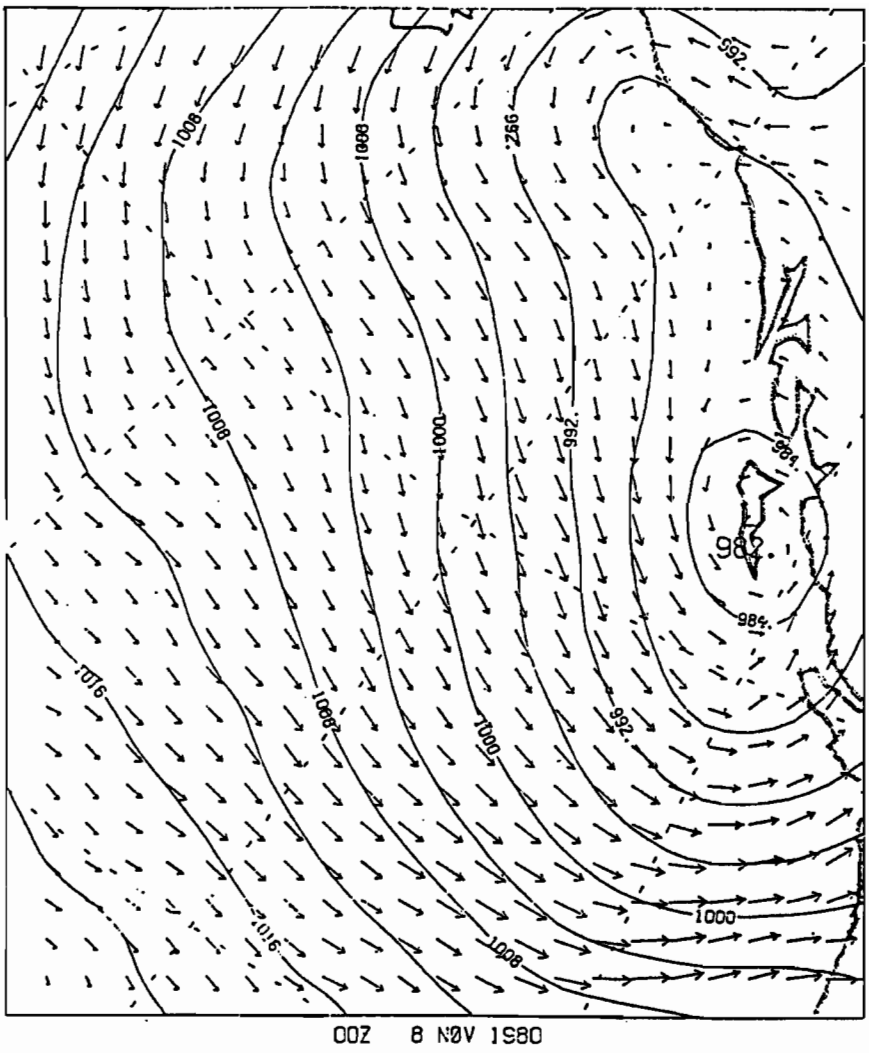

Figure 4.14 Surface boundary layer analysis from Brown's model. Distance between grid points = 20 m s^{-1}.

FLUX MEASUREMENTS OF 7 NOVEMBER 1980

File #	Time GMT	Altitude	U_{alt}	τ/p	$C_{dn} \times 10^{-3}$	U_{10}	L	Tv_{alt}	T_{10}
9	0051	44	9.7	.223	2.7	8.8	-134	9.4	9.8
10	0100	45	8.4	.105	1.7	7.7	-90	8.4	8.8
11	0111	47	8.0	.119	2.1	7.3	-101	8.5	8.9
12	0118	46	5.8	.104	3.0	5.3	-25	6.9	7.4
13	0121	46	9.0	.247	3.3	8.2	-92	7.8	8.3
14	0130	46	8.2	.128	2.0	7.5	-65	7.6	8.1

U_{alt} - mean wind speed at aircraft altitude

C_{dn} - neutral drag coefficient at 10-meters altitude

L - Obukov length

T_v - virtual temperature at aircraft altitude, U_{alt}

T_{10} - virtual temperature at 10-meters altitude

Table 4.3

LASER WAVE SPECTRA 7 NOVEMBER 1980

Laser File Start Time	β x10^{-3}	6 sec energy m^{-2} sec	H 1/3	Peak Freq hz	Long/Lat	Time at center of file	U_{19} in m/sec
0051	6.26	2.24	3.75	.08	141.58/48.74	0055:30	8.8
0100	4.77	1.55	3.59	.08	142.07/48.93	0102:30	7.7
0111	4.29	1.61	3.50	.079	142.79/49.20	0112:30	7.3
0118	3.39	1.37	3.19	.087	143.29/49.38	0119:30	5.4
0121	5.29	1.73	2.99	.082	143.77/49.56	0126:00	8.2
0130	6.08	1.71	3.27	.081	144.46/49.81	0135:30	7.5

Table 4.4

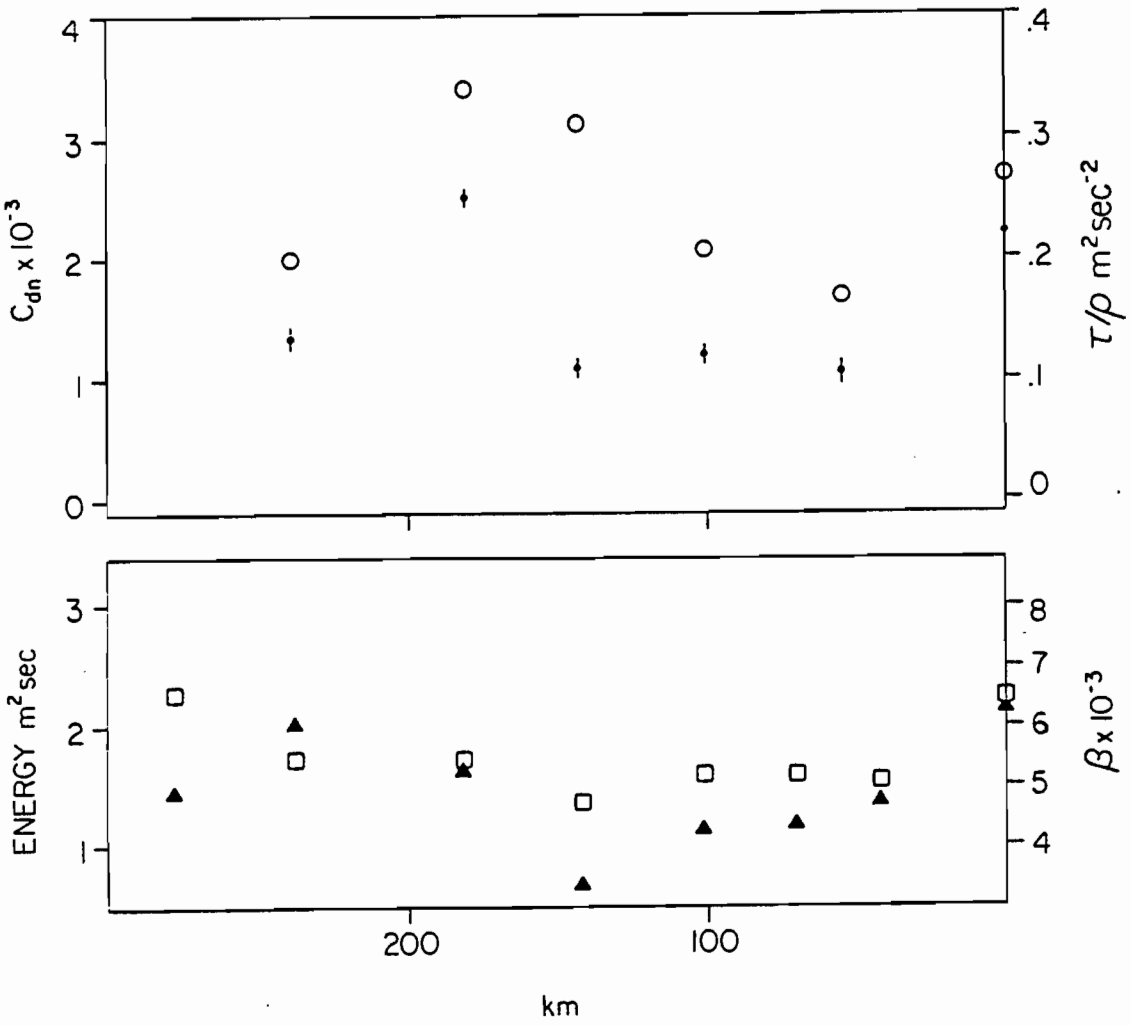

Figure 4.15 *Upper panel*: Drag coefficient C_{dn} o, and τ/ρ, vs upwind track distance for 7 November 1980.

Figure 4.16 *Lower panel*: 6-sec wave energy □ and, β Δ vs upwind track distance for 7 November 1980.

5. CHAPTER V: DISCUSSION

The large body of data we have previously mentioned points to a representation of z_o as occurring according to Charnock's original equation, *i.e.*,

$$z_o \alpha \frac{au_*^2}{g}$$

and, therefore, statistically C_d is a slowly increasing function of wind speed. It appears that there is a dynamic equilibrium situation existing between waves and the overlying wind field. This dynamic equilibrium is characterized by a wave spectral peak frequency whose phase speed is less than or very close to that of U_{10}. The JONSWAP spectra and fetch-limited spectra in general seem to follow this equilibrium. It is within this type of dynamic equilibrium that a representation of z_o in terms of the sea state should converge to Charnock's sea state formulation, and we need a representation of z_o that reflects this. Kutzbach (1961) performed a pilot experiment on wind profile modification on the ice of Lake Mendota (Wisconsin) by varying the number of baskets placed upwind of an anemometer mast. He varied z_o from 10^{-4} m to 10^{-1} m. In a simplification of Kurtzbach's results Lettau (1969) proposed the following representation.

$$z_o = 0.5\, h^* s/S$$

where

h^* is the height of the object	meters
s is its silhouette area	meters^2
S is the specific area	meters^2

This type of representation allows for an additional boundary condition which is equivalent to packing density. In a stationary terrestrial situation this is a straight forward situation and z_o can be computed for any given situation.

It is somewhat different, however, with a mobile underlying surface. I will use Lettau's idea as a starting point to develop a representation of z_o which responds to the underlying wave field.

Suppose we write

$$z_o \alpha f_w h^* s/S$$

where f_w is some "average" drag coefficient

h^* is the wave height

s is the silhouette area

S is the specific area.

For a two dimensional wave field, which is moving in the direction of the prevailing wind, we can show that

$$s = h^* \times \text{width}$$

and the specific area

$$S = \lambda \times \text{width}$$

where λ is the wavelength of the waves.

Therefore, the s/S ratio reduces to the slope of the wave, h^*/λ, for each individual roughness element as it is seen by the wind. Now

$$z_o \alpha f_w \frac{h^* h^*}{\lambda}$$

Also, z is a scaling length which is a result of summing all of the contributions to the roughness scale. We know from deep-water wave theory that

$$c_p = \left(\frac{g\lambda}{2\pi}\right)^{\frac{1}{2}}$$

where c_p is the phase velocity of the wave with wavelength λ. But

$$c_p = \frac{g}{\omega} = \frac{\lambda\omega}{2\pi}$$

or substituting

$$\lambda = \frac{2\pi g}{\omega^2}$$

therefore

$$z_o \alpha \Sigma\left[\frac{f_w h^* h^* \omega^2}{2\pi g}\right]$$

where we sum overall of the roughness elements.

z_o is now expressed as a function of h^* and ω and an undefined drag coefficient. But h^* is $h^*(\omega)$. We know that:

$$h^{*2} \alpha a^2$$

where a^2 is the amplitude squared of the wave. We also know that the rms amplitude squared, a^2 can be written as,

$$a^2 = \int S(\omega)\, d\omega$$

where $S(\omega)$ is the spectral-energy density of the surface waves.

Now

$$z_o \alpha \frac{f_w}{2\pi g}\int S(\omega)\omega^2 d\omega$$

If we are in the dynamic equilibrium situation, we can expect that the wave spectrum will behave according to Phillips' spectral representation

$$S(\omega) = \beta\, g^2\, \omega^{-5} \qquad \omega > \omega_{max}$$

$$S(\omega) = o \qquad \omega < \omega_{max}$$

and ω_{max} is the peak of the wave spectrum. We also expect the peak of the spectrum to be very close to the $\omega = g/U_{10}$. In this situation, the entire energy of the spectrum is characterized by β and the peak frequency ω and we can write

$$z_o \alpha \frac{f_w \beta g^2}{2\pi g} \int_{g/U_{10}}^{\infty} \omega^{-3} d\omega$$

We only want to use the part of the spectrum that moves slower than the wind and let c_o be the phase velocity of the surface waves moving slower than the wind. Since $c_o/u_* \leq 20$ for actively developing waves (Kitaigorodskii, 1970), $c_o \leq 20u_*$, and we could also use $\omega = g/c_o$ as the limit in the integral. Therefore, we can write the integral limit either as g/U_{10} or $g/20u_*$. The integral now becomes

$$z_o \alpha \frac{f_w \beta g^2}{2\pi g} \left[\frac{\omega^{-2}}{2} \right]_{g/U_{10}}^{\infty}$$

or changing the limits of integration;

$$z_o \alpha \frac{f_w}{2\pi g} \beta g^2 \left[\frac{\omega^{-2}}{2} \right]_{\infty}^{g/U_{10}}$$

evaluating the end points we have,

$$z_o \alpha \frac{3f_w\beta g^2}{2\pi g}\left[\frac{U_{10}^2}{g2} - \frac{1}{\infty}\right]$$

or $$z_o \alpha \frac{f_w\beta\ U_{10}^2}{4\pi g}$$

If we had taken the limit to be $g/20u^*$, the functional form of z_o would be

$$z_o \alpha \frac{(200)f_w\beta}{2\pi}\ \frac{u_*^2}{g} = \frac{a'u_*^2}{g}$$

which is the original relation derived by Charnock on dimensional grounds.

We should mention that there was usually some point at a high enough frequency in the spectrum where the remaining spectrum could be modeled by Phillips' relation $S(\omega) = \beta g^2\omega^{-5}$. Usually when $\omega \geq 1.88$.

If, however, the wave field is not in dynamic equilibrium and for some reason cannot be modeled by Phillips' spectra, then the evaluation of z_o would have to proceed differently. For these cases where the spectrum cannot be modeled analytically, the representation for z_o could be written as,

$$z_o \alpha \frac{f_w}{2\pi g}\left[\sum_{\omega_i}^{\omega = 1.88} S(\omega)\omega^2\Delta\omega + \beta g^2 \int_{\omega = 1.88}^{\infty} \omega^{-3} d\omega\right]$$

where ω_i is the frequency of the lowest frequency wave that has a phase velocity less than U_{10}. We can see that we will still have a contribution that will scale as

$$\frac{\beta U^2}{2\pi g} \text{ or } \frac{\beta u_*^2}{2\pi g}$$

from the second term in the brackets. But the additional summation term will weight the roughness elements by the inverse square of the wave speed

$$\omega^2 \alpha \frac{1}{c_p^2}$$

As ω increases from the ω_i toward $\omega = 1.0$, the relative weight of $S(\omega)$ in the nonequilibrium case is not decreasing as fast as ω^{-5}; therefore, the contribution from the first term in the square bracket will always be larger than the equivalent integral calculation, using Phillips' representation. The result is that the representation for z_o will always be larger than if the wave field had the dynamic equilibrium distribution of roughness elements. It is interesting to note that the area where the ω^2 weighting begins to exceed 1 is the beginning of the six-second wave band $\sim$ .159 hz. Therefore, the increase in energy in this band should correlate well with an increase in z_o and C_{dn}.

The measured variability of C_{dn} in the marine surface layer depends on four major variables:

1) instrumental errors

2) sampling errors of a random variable

3) atmospheric geophysical effects such as stability and wind-speed

4) surface roughness is related to the surface-wave heights.

We have seen experimental evidence of large variations in C_{dn}. All of the measurements were made with the same instrumental system. Therefore, it is unlikely that the variations were due to instrument errors.

Sampling errors of a random nature will contribute to the errors of the deduced C_{dn}. Calculations indicated that a random error of $\pm$ 1 m s^{-1} in U_{10} would contribute a 30% error in the calculated value of measured C_{dn}. There were not sufficient data to perform any reasonable statistical processing but indications are that the factor of three change in C_{dn} was well beyond the statistical variability. Error calculations are very difficult in a study which does not have temporal stationarity. Ensemble averaging is the only procedure which is available to reduce the random variations.

Atmospheric effects such as stability were compensated for while the wind speed for the upwind run on the 15 November flight was nearly constant. Figure 5.1 shows the variations in C_{dn} vs. wind speed. It seems that variations in atmospheric effects could not account for the large variations in C_{dn}. Finally, we are left with the surface roughness. As we have seen from the treatment above, departures from the dynamic equilibrium wave spectra produce a spectral distribution of wave energy, which has a tendency to increase z_o and C_{dn}.

Our data analyses show a correlation that supports this treatment. As the wave energy in the six-second (and higher) wave field grows, C_{dn}

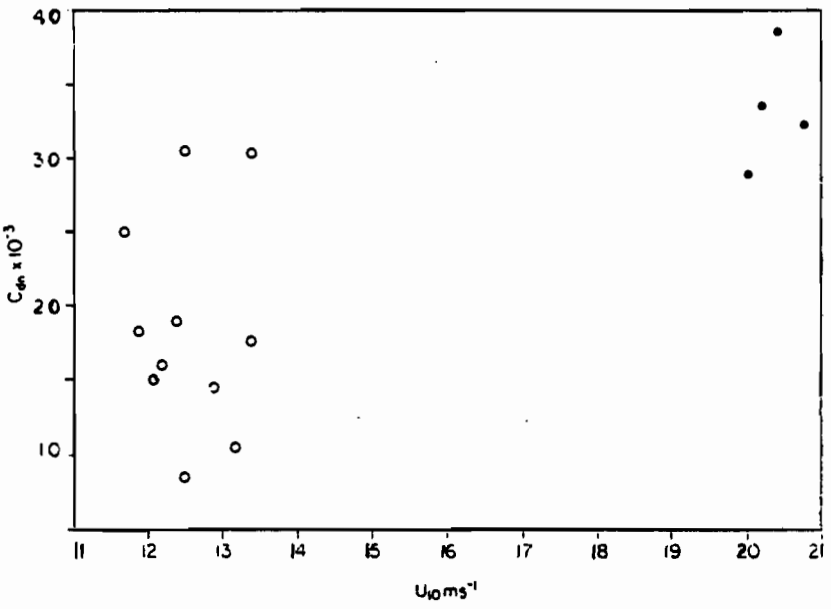

Figure 5.1 C_{dn} vs. U_{10} for 15 November 1980. The solid circles are the measurements made in the warm sector. The open circles are the measurements made in the cold sector behind the front.

was increasing. At the point where the energy in the six-second wave band decreased, C_{dn} started to decrease.

The model contains a single parameter f_w which must be determined by comparison with the data but which should be between 1 and .1. The value for f_w was chosen by looking at the equilibrium wave field in the warm sector of the 15 November storm and setting the f_w such that C_{dn} (waves) was close to C_{dn} measured by the gust probe system. The same value of f_w was then used to evaluate the nonequilibrium wave field in the cold sector of the 15 November storm, and the equilibrium wave field of the 7 November flight. The measured C_{dn} are graphed against the modeled C_{dn} from the wave spectral measurements (Figure 5.2). The points which had the lowest measured C_{dn} were from the stress measurements closest to the front. It would seem that f_w probably is not a constant but is some function of duration (*i.e.*, time since the wind changed direction). However, due to the limited data set all that we can do currently is speculate regarding the form of f_w. For comparison, the measured C_{dn} is graphed against C_{dn} computed using the relationship of Large and Pond (1981) in Figure 5.3. We can see that their relation substantially underestimates the drag for all but the lowest values.

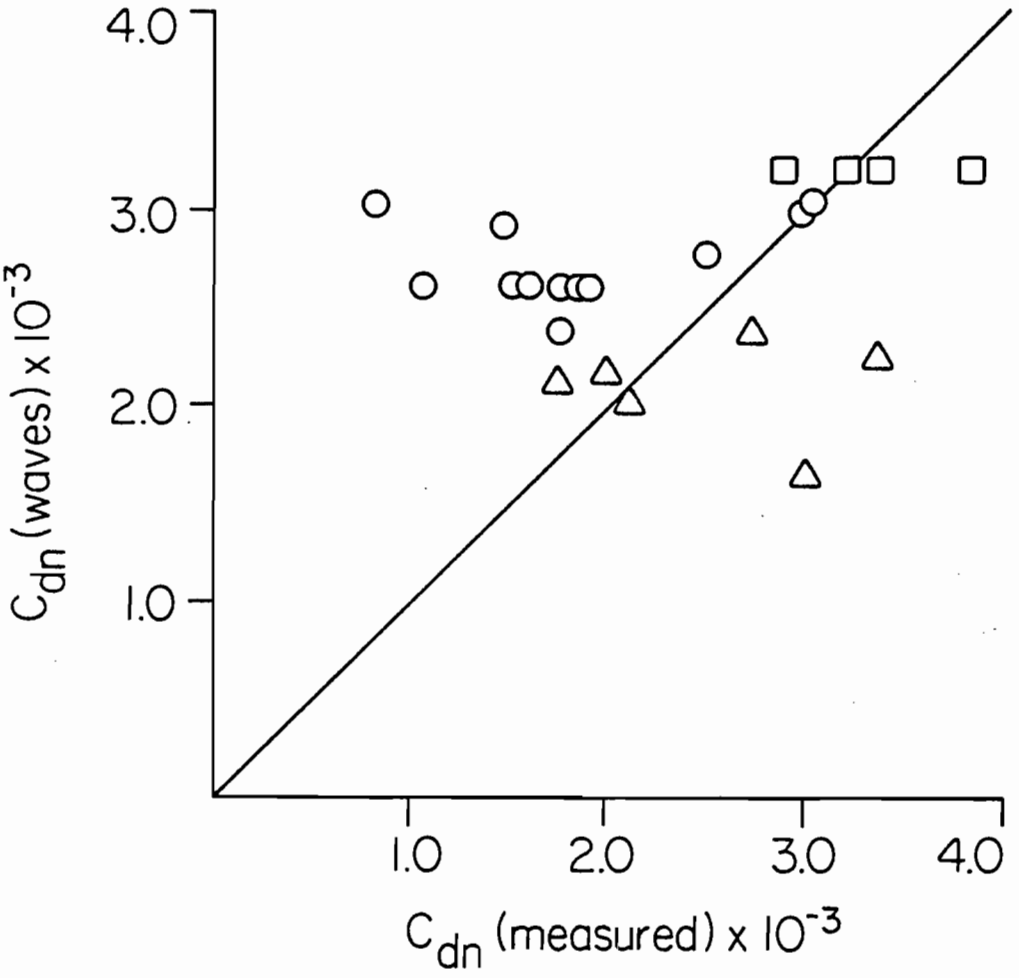

Figure 5.2 Neutral drag coefficient estimates C_{dn} compared with modeled values. The data □ are the 15 November warm sector values, o, are the 15 November cold sector values, Δ are the 7 November values.

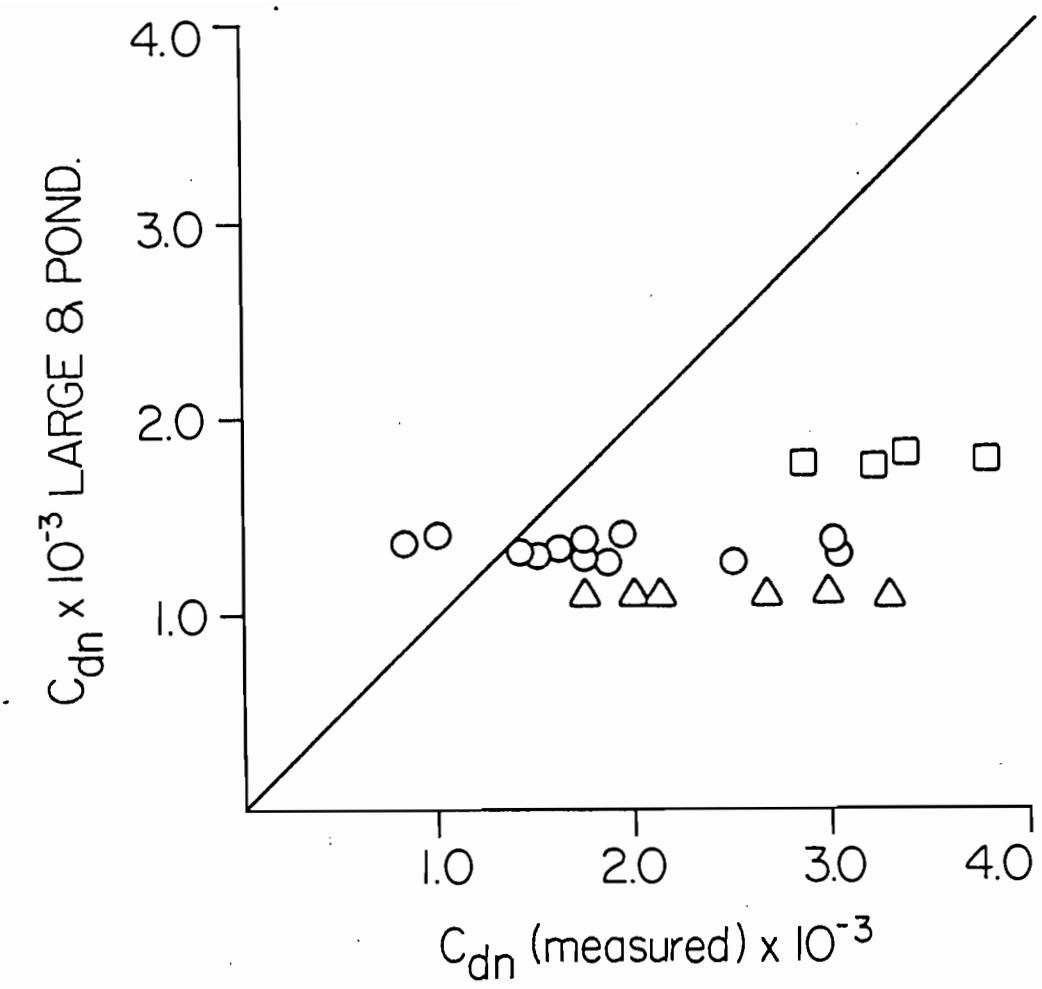

Figure 5.3 Neutral drag coefficients estimates C_{dn} compared with values calculated using the relationship of Large and Pond (1981).

$$10^3 C_{dn} = \begin{cases} 1.12 & 4 \leq U_{10} < 11 \text{ m s}^{-1} \\ .49 + .067U_{10} & 11 \leq U_{10} < 11 \text{ m s}^{-1} \end{cases}$$

The line of perfect agreement is shown (solid) are the warm sector 15 November, o are the cold sector 15 November, Δ are 7 November data.

6. CHAPTER VI. SUMMARY AND RECOMMENDATIONS

We have found that at any given wind speed the measured momentum flux is highly variable and time histories or spatial studies of the winds, surface waves, and eddy correlation fluxes can be used to explore sources of the variability.

Data from the 15 November 1980 experiment show that C_{dn} varied over a large range and that variations exceeded any that could be accounted for by changes in surface wind speed using relationships reported previously in the literature. The wind speed for most of the measurements made in the unstable sector was nearly constant (to within ± 1 m/sec), the variations of C_{dn} with changes in surface wave spectrum were larger than the variations in C_{dn} from the warm sector with 20-22 m/sec winds to the cold sector with 12-13.5 m/sec winds. We found C_{dn} to be a slightly increasing function of U_{10} but, as above, with excessive scatter in the data points. Previous work, which attempted to relate drag coefficients to surface wind speed, paid slight attention to the coincident surface wave field. As this work was being completed, it came to our attention that Donelan (1982) has developed an empirical relation between C_{dn} and U_{10} using the peak frequency of the wave field and wave hindcasting to allow for wave effects. Our investigation, which measured the complete one-dimensional surface wave spectrum, constitutes the first time wave spectral measurements have been made together with eddy correlation flux measurements in the marine surface layer.

The data sets used during the study are unique in the measurement of momentum flux, bulk wind speed and temperature, and surface wave spectra. This measurement group includes all of the variables needed to check the relations of C_{dn} to z_o.

The wave spectral energy distribution in the duration-limited sea region behind the 15 November front was found to differ markedly from the energy distribution of a fetch-limited case. The short gravity waves continued to increase in energy with increasing distance behind the front.

Variations in the drag coefficient, C_{dn}, measured in the cold sector of the 15 November storm, appeared to be well correlated with the in energy in these short gravity waves.

Using only the wave spectral information, we derived a representation of z_o, which reduced to Charnock's relation in situations of dynamic equilibrium between the wind field and the surface waves. In situations of disequilibrium between the wave field and the surface wind, the derived relation shows a strong dependence of z_o on the six-second wave field. We found that the C_{dn} calculated from measurements made during the 15 November 1980 frontal penetration followed the derived z_o relationship. This relationship of z_o to the surface wave spectra helps explain the apparently high values of C_{dn} behind moving fronts which have been reported in the literature.

We found that Phillips' parameter β, has a tendency to increase with wind speed, but we also note that variations in β at a particular wind speed, but differing wave states, exceed the maximum excursions due to changes in wind speed.

We found that β increases very rapidly immediately behind a front before returning to a lower equilibrium value. This large rise and fall of energy in the saturated region of the wave field may account for the ability of radar scatterometers to easily locate atmospheric frontal signatures.

Unfortunately, we were unable, due to instrument failures, to investigate the two-dimensional aspects of the surface wave/atmospheric surface layer interaction. This is a problem that will have to be addressed when more data become available.

Both case studies were in regions of moderate instability in the cold sectors. It was in the cold sectors that we saw the large variations. In the warm sector, with high winds, the surface wave spectra were nearly in dynamic equilibrium with the spectral peak frequency. This situation had C_d values closest to the "normal" values found in the literature.

There were some reservations about using diabatic correction functions which had been developed from terrestrial experiments, and the question of whether von Karman's constant should be 0.4 or 0.35. Investigation of the ψ functions and von Karman's constant in a marine environment would be a useful undertaking. Perhaps the equivalent of the Kansas experiment could be undertaken on a tidal flat to determine if there is a substantial change in diabatic wind profile shape with or without the water boundary.

Recommendations for Future Work

Measurements of the two dimensionality of the wave field should be made where it was assumed in this study. This would provide a func-

tional representation of s/S which most likely will have some dependence on wind speed and duration of the new wind field.

The eddy correlation drag measurements and wave field measurements should be carried out over a wider range of wind speeds. This would be especially important in a case where U_{10} behind the front was less than 7-8 m/sec which marks the onset of white capping. An experiment to measure concurrently the surface layer momentum flux, the bulk wind speed, surface wave field, and radar backscatter would be useful. This set of measurements would allow us to make an assessment of the importance of β to radar backscattering cross section.

An experiment which provides all of the above information could be designed using the NOAA P-3 aircraft instrumented as in STREX with side-looking radar to measure the two-dimensional wave field, and the NASA C-130 carrying a radar scatterometer.

These two aircraft could operate in a region off the California coast, overflying the NDBO disk buoy which make hourly wave spectral measurements and surface meteorological measurements. The two aircraft would be well suited to intercept incoming frontal systems and gather data for a significant range of wind speeds and atmospheric conditions. This study would also be very useful in establishing the growth patterns of duration limited seas.

According to Hasselmann (1976), the shape of the atmospheric input function to wave generation models appears to depend on the shape of the surface wave spectrum. Our results indicate that the drag coefficient which couples the surface layer bulk measurements to momentum flux is a very sensitive function of the relative balance of surface wind speed, the distribution of wave spectral energy and wave phase

velocity. A detailed exposition of the functional relationship will require more data (including two dimensional data) than now exists. However, it does appear that in the turning wind conditions, the increase in wave spectral energy in the shorter gravity wave region behind the spectral peak makes a two-parameter representation of the wave field inadequate.

Finally, the large variations in C_d, correlated with changes in the surface wave spectra, indicate that wave spectral measurements should always accompany marine micrometeorological investigations.

7. REFERENCES

Barnett, T.P., On the generation, dissipation, and prediction of ocean wind waves. J. Geophys. Res., 73, 513-530, 1968.

Barnett, T.P., and J.C. Wilkerson, On the generation of ocean wind waves as inferred from airborne radar measurements of fetch-limited spectra, J. Mar. Res., 25, 292-328, 1967.

Bean, B.R., and C.B. Emmanuel, Aircraft in Air Sea Interaction, edited F. Dobson, L. Hasse, R. Davis, Plenum Press, N.Y., 1980.

Bondarenko, I.M., A.A. Zagorodnikov, V.S. Loschchilov, and K.B. Tchelyshev, The relationship between wave parameters and the spatial spectrum of aerial- and radar-pictures of the sea surface, Okeanologiya, XII(6), 1972.

Bogorodskii, M.D., Issledovanie tangentsial'nogo treniya, vertikal' nogo turbulentnogo teploobmena i ispareniya v usloviyakh otkrytogo (Investigations of Tangential Friction, Vertical Turbulent Heat Exchange and Evaporation in Conditions of the Open Ocean). - Okeanologiya, 4(1), 1964.

Brown, R.A., Model derived wind fields for STREX, unpublished manuscript, University of Washington Polar Science Center, 1982.

Busch, N.E., Fluxes in the surface boundary layer over the sea, in Modeling and Prediction of the Upper Layer of the Ocean, edited by E.B. Kraus, Pergamon Press, N.Y., 1977.

Businger, J.A., J.C. Wyngaard, Y. Izumi, Flux profile relationships in the atmospheric surface layer, J. Atmos. Sci., 28, 181-189, 1971.

Byrne, H.M., A versatile record-keeping mechanism for on line geophysical data, unpublished manuscript, NOAA ERL-PMEL, Seattle, Wash., 1982.

Cardone, V.J., Specification of the wind field distribution in the marine boundary layer for wave forecasting, Rept. TR69-1, Geophys. Sci. Lab., New York University, 1969.

Charnock, H., Wind stress on a water surface, Quart. J. Roy. Meteorol. Soc., 81, 639, 1955.

Deacon, E.L., P.A. Sheppard, and E.K. Webb, Wind profiles the sea and the drag at the sea surface, Aust. J. Phys., 9(4), 1956.

Deardorff, J.W., Dependence of air-sea transfer coefficients on bulk stability, J. Geophys. Res., 73, 2549-2557, 1968.

Denman, K.L. and M. Miyake, The behavior of the mean wind, the drag coefficient, and the wave field in the open ocean, J. Geophys. Res., 78, 1917-1931, 1973.

Dobson, F.W., Measurements of atmospheric pressure on wind-generated sea waves. J. Fluid Mech., 48, 91-127, 1971.

Donelan, M.A., F.C. Elder, and P.F. Hamblin, Determination of the aerodynamic drag co-efficient from wind set-up. Proc. 17th Conf. Great Lakes Research Int. Assoc. Great Lakes Res., 778-788, 1974.

Donelan, M.A., Are aquatic micrometeorologists delivering the goods or is the over-water drag coefficient far from constant?, in Symposium of Transport Mechanisms in Oceans and Lakes, Marine Environmental Data Service, Department of the Environment, Ottawa, Ontario, 1975.

Donelan, M.A., The dependence of the aerodynamic drag coefficient on wave parameters. National Water Research Institute, Canada Centre for Inland Water, Burlington, Ontario, Canada, unpublished manuscript, 1982.

Dorrestein, R., and P. Grosen, Zsegkven, Kon, Nat. Met. Inst. Rept. No. II, 1958.

Dyer, A. J., A review of flux-profile relationships, Bound. Layer Meteor., 7, 363-372.

Fleagle, R.G., J.W. Deardorff, and F.L. Badgley, Vertical distribution of wind speed, temperature and humidity above a water surface, J. Mar. Res., 17, 141-157, 1958.

Fleagle, R.G., and J.A. Businger, An introduction to atmospheric physics. Academic Press, N.Y., 1980.

Fleagle, R.G., M. Miyake, J.F. Garrett, and G.A. McBean, Storm transfer and response experiment, Bull. Amer. Met. Soc., 63(1), 6-14, 1982.

Garrett, J.R., Review of drag coefficients over oceans and continents, Mon. Wea. Rev., 105, 915-929, 1977.

Goptarev, N.N., Nekotorye rezul'taty gradientnykh issledovanii v raione Neftyanykh Kamnei (Some results of wind profile measurements in the Nefyanye Kamni region), Trudy GOINa, 36, 1957.

Hasse, L., M. Gruenwald, and D.E. Hasselmann, Field Observations of Air Flow above the Waves in Turbulent Fluxes through the Sea Surface, Wave Dynamics, and Prediction, edited by A. Favre and K. Hasselmann, Plenum Press, 1977.

Hay, D.R., Fast response humidity sensors in Air Sea Interaction, edited by F. Dobson, L. Hasse, R. Davis, Plenum Press, N.Y., 1980.

Hasselmann, D.D., M. Dunckel, and J.A. Ewing, Directional wave spectra observed during JONSWAP, (1973), J. Phys. Oceanog., 10(8), 1264-1280, 1980.

Hasselmann, K., D.B. Ross, P. Muller, and W. Sell, A parametric wave prediction model, J. Phys. Oceanogr., 6(2), 200-228, 1976.

Hasselmann, K., On the spectral dissipation of ocean waves due to white-capping, Bound.-Layer Meteor., 6, 107-127, 1974.

Hasselmann, K., R.P. Barnett, E. Bouws, H. Carlsen, D.E. Cartwright, A. Meerburg, P. Müller, D.J. Olbers, K. Richter, W. Sell, and H. Walden, Measurements of wind-wave growth and swell decay during the joint north sea wave project (JONSWAP), Ergänzungsheft zur Deutschen Hydrographischen Zeitschrift, A(i°), (12), 1973.

Hasselmann, K., The energy balance of wind waves and the remote sensing problem, NOAA Tech. Rept. ERL 228-AOML 7-2, 25-1, 25-55, 1972.

Hsu, S.A., A dynamic roughness equation and its application to wind stress determination at the air-sea interface, J. Phys. Oceanogr., Vol. 4, 116-120, 1974.

Jenkins, G.M., and D.G. Watts, Spectral Analysis and its Applications, Holden-Day, San Franscisco, 525 pp., 1969.

Kinsman, B., Wind Waves, Prentice-Hall, Englewood Cliffs, N.J., 675 pp., 1965.

Kitaigorodskii, S.A., On the calculation of the aerodynamic roughness of the sea surface, Izv. Atmos. Oceanic Phys., 4, 498-502, 1968.

Kitaigorodskii, S.A., The physics of air-sea interaction, tr. from Russian by A. Baruch, Israel Program for Scientific Translations, Jerusalem, 1973.

Kitaigorodskii, S.A., and M.M. Zaslavskii, A dynamical analysis of the drag conditions at sea surface, Bound.-Layer Meteorol., 6, 53-61, 1974.

Kondo, J., Y. Fujunawa, and G. Naito, High frequency components of ocean waves and their relation to the aerodynamic roughness, J. Phys. Oceanog., 3, 197-202, 1973.

Kondo, J., Air sea bulk transfer coefficients in diabatic conditions, Bound.-Layer Meteorol., 91-112, 1975.

Kraus, E.B., Aerodynamic roughness over the sea surface, J. Atmos. Sci., 23, 443-445, 1966.

Kraus, E.B., What we do not know about the sea surface wind stress, Inst. Atmos. Sci., Univ. of Miami, Publication No. 1, 1967.

Krugermeyer, L., M. Gruenwald, and M. Dunkel, The influence of sea waves on the wind profile, Bound.-Layer Meteorol., 14, 403-414, 1978.

Kutzbach, J., Investigations of the modification of wind profiles by artifically controlled surface roughness. Studies of the three dimensional structure of the planetary boundary layer, Annual Rept. 1961, Dept. of Meteorol., University of Wisconsin, Madison, 71-113, 1961.

Large, W.G., and S. Pond, Open ocean momentum flux measurements in moderate to strong winds, J. Phys. Oceanogr., 11, 324-336, 1981.

Lettau, H., Note on aerodynamic roughness-parameter estimation on the basis of roughness-element description, J. Appl. Met., 8, 828-832, 1969.

Liu, P.C., and D.B. Ross, Airborne measurements of wave growth for stable and unstable atmospheres in Lake Michigan, J. Phys. Oceanogr., 10, 1980.

Liu, P.C., Normalized and equilibrium spectra of wind waves in Lake Michigan, J. Phys. Oceanogr., 1, 249-257, 1971.

Long, R.B., On surface gravity wave spectra observed in a moving frame of reference, NOAA Tech. Memo. ERL-AOML-38, 1979.

Longuet-Higgins, M.S., D.E. Cartwright, and N.D. Smith, Observations of the directional spectrum of sea waves using the motions of a floating buoy. Proc. Conf. Ocean Wave Spectra., Prentice-Hall, 111-136, 1973.

Miles, J.W., On the generation of surface waves by shear flows. J. Fluid Mech., 3, 185-204, 1957.

Mitsuyasu, H., F. Tasai, T. Suhara, S. Mizuno, M. Ohkusu, T. Honda, and R. Rikiishi, Observations of the directional spectrum of ocean waves using a cloverleaf buoy, J. Phys. Oceanogr., 5, 750-760, 1975.

Monin A.S. and A.M. Yaglom, Statistical Fluid Mechanics. Mechanics of Turbulence, edited by John L. Lumley, 2 vols., M.I.T. Press, 1971-75.

NATA AGARDOGRAPH 139, Theory and applications of Kalman filtering, edited by C.T. Leondes, North Atlantic Treaty Organization Advisory Group for Aerospace Research and Development, 7 rue Ancelle 92200, Neuilly sur Seine, France, 1970.

Nikuradse, J., Stromungsgesetze in rauhen Rohren, VDI Forschungsheft, No. 361. NACA translation, 1933.

Phillips, O.M., The dynamics of the upper ocean, Cambridge Univ. Press, 336 pp., 1980.

Phillips, O.M., The structure of short gravity waves on the ocean surface in Spacebourne synthetic aperture radar for oceanography, edited by R.C. Beal et al., John Hopkins Press, Baltimore, 1981.

Pierson, W.J., Jr., and L. Moskowitz, A proposed spectral form for fully developed wind seas based on the similarity theory of S.A. Kitaigorodskii, J. Geophys. Res., 69, 5181-5190, 1964.

Pierson, W.J., Verification procedures for SEASAT measurements of the vector wind with the SASS, report to Jet Propulsion Laboratory Contract No. 9554411, City Univ. of New York, NTIS No. AD-A0703 644/7ST, 1978.

Pond, S., Some effects of buoy motion on measurements of wind speed and stress, J. Geophy. Res., 73, 507-512, 1968.

Reynolds, R.M., Surface and meteorological observations by ship and toroid buoy in the North Pacific during STREX, a comparison, unpublished manuscript, NOAA ERL-PMEL, Seattle, Wash., 1982.

Roll, H.U., Basic concepts of the physics of the marine atmosphere, 7, Academic Press, N.Y., 1965.

Ross, D.B., V.J. Cardone, and J.W. Conaway, Jr., Laser and microwave observations of sea-surface conditions for fetch-limited 17- to 25-m/s winds, IEEE Trans., vol. GE-8, No. 4, 326-336, 1970.

Ross, D.B., and V.J. Cardone, Observations of oceanic whitecaps and their relation to remote measurements of surface wind speed, J. Geophys. Res., 79(3), 444-452, 1974.

Ross, D.B., On the use of aircraft in the observation of one and two dimensional ocean wave spectra in ocean wave climate, edited by M.D. Earle and A. Malahoff, Plenum Press, N.Y., 1977.

Ross, D.B., Aircraft wave spectra observation in Proc. of the Ocean Wave Climate Symposium, edited by A. Malahoff, Plenum Press, N.Y., 1979.

Ruggles, K.W., The vertical mean wind profile over the ocean for light to moderate winds, J. of Applied Met., 9(3):389-395, 1970.

Schlichting, H., Boundary-Layer Theory, translated from German by J. Kestin, 6th ed., McGraw-Hill, 6th Ed., New York, 747 pp., 1968.

SethuRaman, S., and G.S. Raynor, Surface drag coefficient dependence on the aerodynamic roughness of the sea, J. Geophy. Res., 80, 4983-4988, 1975.

SethuRaman, S., Influence of mean wind direction on sea surface wave development, J. Phys. Oceanog., 8, 926-929, 1978b.

Smith, S.D., and E.G. Banke, Variation of the sea surface drag coefficient with wind speed, Quart. J. Roy. Met. Soc., 101, 665-673, 1975.

Stewart, R.W., The wave drag of wind over water, J. Fluid Mech., 10, 189-194, 1961.